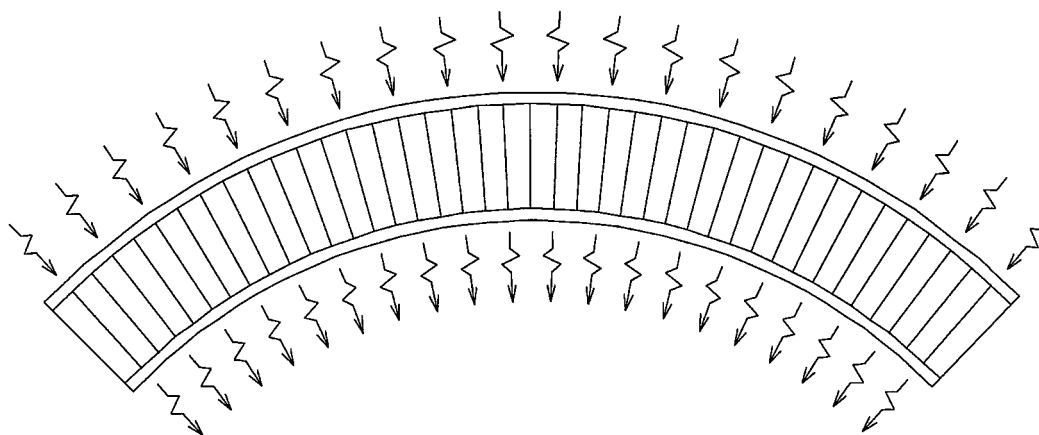# Open-Mode Debonding Analysis of Curved Sandwich Panels Subjected to Heating and Cryogenic Cooling on Opposite Faces

William L. Ko
Dryden Flight Research Center
Edwards, California

The NASA STI Program Office . . . in Profile

Since its founding, NASA has been dedicated to the advancement of aeronautics and space science. The NASA Scientific and Technical Information (STI) Program Office plays a key part in helping NASA maintain this important role.

The NASA STI Program Office is operated by Langley Research Center, the lead center for NASA's scientific and technical information. The NASA STI Program Office provides access to the NASA STI Database, the largest collection of aeronautical and space science STI in the world. The Program Office is also NASA's institutional mechanism for disseminating the results of its research and development activities. These results are published by NASA in the NASA STI Report Series, which includes the following report types:

- TECHNICAL PUBLICATION. Reports of completed research or a major significant phase of research that present the results of NASA programs and include extensive data or theoretical analysis. Includes compilations of significant scientific and technical data and information deemed to be of continuing reference value. NASA's counterpart of peer-reviewed formal professional papers but has less stringent limitations on manuscript length and extent of graphic presentations.

- TECHNICAL MEMORANDUM. Scientific and technical findings that are preliminary or of specialized interest, e.g., quick release reports, working papers, and bibliographies that contain minimal annotation. Does not contain extensive analysis.

- CONTRACTOR REPORT. Scientific and technical findings by NASA-sponsored contractors and grantees.

- CONFERENCE PUBLICATION. Collected papers from scientific and technical conferences, symposia, seminars, or other meetings sponsored or cosponsored by NASA.

- SPECIAL PUBLICATION. Scientific, technical, or historical information from NASA programs, projects, and mission, often concerned with subjects having substantial public interest.

- TECHNICAL TRANSLATION. English-language translations of foreign scientific and technical material pertinent to NASA's mission.

Specialized services that complement the STI Program Office's diverse offerings include creating custom thesauri, building customized databases, organizing and publishing research results . . . even providing videos.

For more information about the NASA STI Program Office, see the following:

- Access the NASA STI Program Home Page at *http://www.sti.nasa.gov*

- E-mail your question via the Internet to help@sti.nasa.gov

- Fax your question to the NASA Access Help Desk at (301) 621-0134

- Telephone the NASA Access Help Desk at (301) 621-0390

- Write to:
  NASA Access Help Desk
  NASA Center for AeroSpace Information
  7121 Standard Drive
  Hanover, MD 21076-1320
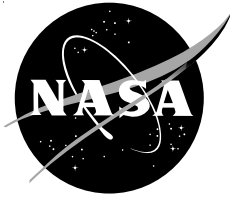
Open-Mode Debonding Analysis of Curved Sandwich Panels Subjected to Heating and Cryogenic Cooling on Opposite Faces

William L. Ko
Dryden Flight Research Center
Edwards, California

Available from the following:

CONTENTS

ABSTRACT

Increasing use of curved sandwich panels as aerospace structure components makes it vital to fully understand their thermostructural behavior and identify key factors affecting the open-mode debonding failure. Open-mode debonding analysis is performed on a family of curved honeycomb-core sandwich panels with different radii of curvature. The curved sandwich panels are either simply supported or clamped, and are subjected to uniform heating on the convex side and uniform cryogenic cooling on the concave side. The finite-element method was used to study the effects of panel curvature and boundary condition on the open-mode stress (radial tensile stress) and displacement fields in the curved sandwich panels. The critical stress point, where potential debonding failure could initiate, was found to be at the midspan (or outer span) of the inner bonding interface between the sandwich core and face sheet on the concave side, depending on the boundary condition and panel curvature. Open-mode stress increases with increasing panel curvature, reaching a maximum value at certain high curvature, and then decreases slightly as the panel curvature continues to increase and approach that of quarter circle. Changing the boundary condition from simply supported to clamped reduces the magnitudes of open-mode stresses and the associated sandwich core depth stretching.

NOMENCLATURE

A_c	cross-sectional area of honeycomb cell (normal to honeycomb cell generatrix), in^2
A_w	cross-sectional area of honeycomb cell wall (normal to the honeycomb cell generatrix), in^2
E	Young's modulus of face-sheet material, lb/in^2
E_{11}, E_{22}, E_{33}	effective moduli of elasticity of honeycomb core, lb/in^2
E22	beam element for which the intrinsic stiffness matrix is given
E41	quadrilateral membrane element
E43	quadrilateral combined membrane and bending element
G	shear modulus of face-sheet material, lb/in^2
G_{12}, G_{23}, G_{31}	effective shear moduli of honeycomb core, lb/in^2
h	depth of honeycomb core, in.
JLOC	joint location (grid point) of finite-element model
l	half-span curved length along center line of curved sandwich panel, in.
r	$= 57.3\ (l/\theta)$, radius of curved sandwich panel, in.
SPAR	Structural Performance And Resizing finite-element computer program
TPS	thermal protection system
T_l	temperature of concave (lower) surface of curved sandwich panel, °F
T_u	temperature of convex (upper) surface of curved sandwich panel, °F
t_s	thickness of face sheets, in.
α	coefficients of thermal expansion of face sheets, in/in-°F
α_1, α_2, α_3	coefficients of thermal expansion of honeycomb core, in/in-°F

δ_o	radial displacement of middle surface at midspan of curved sandwich panel, in.
Δh	change of honeycomb core depth h (positive for stretching), in.
$(\Delta h)_{max}$	maximum value of Δh, in.
θ	curvature angle (or half-span angle), deg
ν	Poisson's ratio
ρ	weight density of material used for face sheets and honeycomb core, lb/in^3
ρ_{hc}	effective weight density of honeycomb core structure, lb/in^3
σ_r	radial tensile stress (open-mode stress) in honeycomb core cell wall, lb/in^2
σ_θ^l	tangential stress in concave side (lower) face sheet, lb/in^2
σ_θ^u	tangential stress in convex side (upper) face sheet, lb/in^2
$(\sigma_r)_{eff}$	effective radial tensile stress in honeycomb core, lb/in^2
$(\sigma_r)_d$	local maximum value of σ_r in a distribution of σ_r along core depth at a tangential station, lb/in^2
$(\sigma_r)_{max}$	maximum value of $(\sigma_r)_d$, lb/in^2

Subscripts

1, 2, 3	radial, tangential, and axial (longitudinal) directions

INTRODUCTION

Since the well-known successful aerospace application of sandwich structures in the all-wood-constructed British Mosquito fighter-bomber aircraft during World War II (refs. 1–4), the use of sandwich structural technology has become widespread in various aerospace structural applications (e.g., wings, tails, wall panels, webs of beams). The typical sandwich structure in panel form is fabricated with two relatively thin, high-strength face sheets separated by and bonded to opposite sides of relatively thick, low-density, low-strength core. The resulting sandwich structures are lightweight and have high flexural stiffness.

In most aerospace applications, the sandwich panels are curved (e.g., fuselage glove of space shuttle orbiter, certain landing gear doors) or flat with constant core depth or variable core depths to form aerodynamic shapes (e.g., rotary wing blades, T-38 horizontal stabilizers). When applied to hypersonic flight vehicles such as space shuttle orbiter structures that are subjected to severe aerodynamic heating, the sandwich structures are protected with a thermal protection system (TPS) so that the structures can operate in warm temperatures with low thermal gradient across the sandwich core depth (ref. 5). If the thermal gradients across the core depth are too severe, the induced thermal moment could become strong enough to bend the sandwich panel and disturb the original panel shapes. Ko (ref. 6) studied this problem in great detail.

The most extensively used sandwich structure in aerospace technology is the honeycomb-core sandwich structure. Because the honeycomb cell generatrix (a line whose motion generates a honeycomb cell wall) is perpendicular to the face sheets, only line contact ensures proper bonding between the face sheets and the honeycomb core. Corrosion or excess open-mode deformation (moving apart of two face

2

sheets because of bending) can cause the line-contact bonding to lose its integrity—a major drawback of the honeycomb sandwich structure. For titanium alloys, the so-called superplastically-formed/diffusion-bonding fabrication process could be used to form sandwich panels with a variety of core geometries and achieve diffusion-bonded surface contact between the face sheets and sandwich core.

If the sandwich panel is curved, the mechanical or thermal bending in the direction of reducing the panel curvature could induce tensile stress (called *open-mode stress*) in the sandwich core depth direction because the two face sheets tend to separate from each other, causing potential debonding between the face sheets and sandwich core. For the solid curved beams (monolithic or laminated composites) subjected to open-mode bending, the open-mode stress distribution in the curved beam depth direction is arch-shaped; that is, zero values occur at the inner and outer boundaries and the maximum value occurs inward of the middle surface (refs. 7 through 15). The location of the maximum open-mode stress point moves toward the middle surface as the curved beam depth decreases (refs. 7, 8, 15). For a curved (horse-shoe-shaped or semi-elliptic-shaped) sandwich beam subjected to open-mode mechanical bending, however, distribution of the open-mode stress along the core depth direction is almost linear, with the value reaching a maximum at the inner bonding interface (between the sandwich core and face sheets), and tapering down slightly toward the outer bonding interface (ref. 16).

If the open-mode bending is too severe, this unfavorable location of the maximum open-mode stress point in the curve sandwich panel will be the debonding crack nucleation site for inducing the catastrophic debonding failure of the panels. One of the past catastrophic failures of the curved sandwich panels occurred in the honeycomb landing gear door panels of a certain rotary-wing aircraft. During the landing approach when the landing gear doors were wide open, a strong gust of wind induced excess open-mode bending, and caused a catastrophic debonding failure, resulting in the total loss of one of the landing gear doors. Recently, the curved sandwich panels have been designed to reinforce the nozzle ramps of certain nonconventional rocket engines. In such application, the curved sandwich panels will be subjected to open-mode thermocryogenic bending because the convex side of the curved sandwich panels will be exposed to higher temperatures, and the concave side to cryogenic temperatures.

Increasing use of curved sandwich panels as aerospace structure components makes it vital to fully understand their thermostructural behavior and identify key factors affecting the open-mode debonding failure.

This report concerns the finite-element, open-mode debonding analysis of curved honeycomb-core sandwich panels subjected to thermocryogenic bending. The results of the analysis show how the open-mode stress distributions and sandwich panel deformations vary with the panel curvature and boundary condition. The information in this report could serve as guidelines in the effective design of failure-free curved sandwich panels that must function under thermocryogenic environment.

DESCRIPTION OF PROBLEM

The following sections describe the geometry of the family of curved sandwich panels, boundary conditions, and thermocryogenic loading condition used in the analysis.

Geometry

Figure 1 shows a cross-section of the curved honeycomb-core sandwich panel with core depth h, identical face-sheet thickness t_s, half-span curve length l (measured along the center line), radius of curvature r, and the curvature angle (or half-span angle) θ. Panels with different curvatures are

generated by simply changing θ and keeping h, l, and t_s constant. Dimension r automatically changes with θ according to $r = 57.3(l/\theta)$ because l is constant. Table 1 lists the dimensions of the analyzed sandwich panels.

Table 1. Geometry of curved sandwich panels.

h	=	1.4 in.					
l	=	31 in.					
t_s	=	0.032 in.					
θ	=	90° ($r = 19.74$ in.),	75° ($r = 23.68$ in.),	60° ($r = 29.60$ in.),	45° ($r = 39.47$ in.),		
		30° ($r = 59.21$ in.),	15° ($r = 118.41$ in.),	5° ($r = 355.23$ in.),	0° ($r = \infty$, flat)		

The linear dimensions in table 1 (θ excluded) are similar to those of the curved honeycomb-core sandwich panels proposed for reinforcing the nozzle ramps of certain nonconventional rocket engines for future space transportation systems. In the range of $15° > \theta > 0°$, panel deformed shapes for additional curvature angles $\theta = 2.5°$, $6.25°$, $7.5°$, $10°$, and $12.5°$ also were examined to find the critical curvature angle θ at which the panel deformed modal shape changes.

Boundary Conditions

The edges of the curved sandwich panels are either simply supported (fig. 2(a)) or clamped (fig. 2(b)). The method of simply supporting a sandwich panel is slightly different from the conventional way of simply supporting a solid panel. At the sandwich panel edges (fig. 2(a)), transverse rigid bars are attached and pin-joined to the sandwich edges, with the bar midpoints pinned to fixed points lying in the middle surface of the sandwich panel. This method of edge support allows (1) panel edges to rotate freely with respect to the horizontal axes (i.e., edges of middle surface), (2) panel edge depth to remain straight after deformation, and (3) maximum transverse shear deformation to take place at the panel edges. For the clamped boundary condition (fig. 2(b)), the two face sheets and sandwich core at the panel edges are clamped.

Thermocryogenic Loading

The curved sandwich panel is subjected to thermocryogenic loading. The convex side (upper surface) of the sandwich panel is uniformly heated to temperature $T_u = 280$ °F, and the concave side (lower surface) uniformly cooled to cryogenic temperature $T_l = -320$ °F. This temperature range is typical for laboratory testing the structural integrity of curved sandwich panels designed to reinforce the nozzle ramps of certain nonconventional rocket engines. Such thermocryogenic loading certainly induces open-mode bending, and raises concern about potential open-mode debonding failure of the curved sandwich panels.

FINITE-ELEMENT ANALYSIS

The following sections describe the finite-element modeling of the curved sandwich panels, and the material properties used for the face sheets and honeycomb core elements.

4

Finite-Element Modeling

The open-mode linear elastic debonding analysis used the Structural Performance And Resizing (SPAR) finite-element computer code (ref. 17). For simplicity, only a segment of each curved honeycomb-core sandwich panel was considered. Thus, the problem became two dimensional. Because of symmetry with respect to the y-axis (fig. 1), only a semi-span of the curved sandwich panel segment was modeled. Each face sheet was modeled with one layer of isotropic quadrilateral combined membrane and bending E43 elements, and the sandwich core with eight layers of anisotropic quadrilateral membrane E41 elements.

To simulate the pinned rigid rod at the panel edge (fig.2(a)), each node at the edge of the semispan model was pin-connected to the fixed supporting point lying in the middle surface using beam E22 element (for which the intrinsic stiffness matrix is given). The stiffness of the E22 elements was made very large to simulate the rigid rods. Temperature distribution along the sandwich core depth was assumed to be linear. Figure 3 shows a semi-span, finite-element model generated for curved sandwich panel segment with curvature angle $\theta = 90°$. Finite-element models for different panel curvatures were generated from the $\theta = 90°$ model by simply changing the curvature angle θ and the associated radius of curvature r without disturbing other dimensions. Thus, the total number of joint locations (JLOC) and of finite elements remained unchanged. Table 2 lists the size of the finite-element model for any curvature angle θ.

Table 2. Size of finite-element model for any curvature angle θ.

JLOC	2211
E41 elements	1600
E43 elements	400
E22 elements (simply supported case only)	10

Material Properties

The material properties of the face sheets and the honeycomb core used for the finite-element models are of certain age-hardened steel, and are given, respectively, in tables 3 and 4.

Table 3. Material properties of face sheets (age-hardened steel).

	70 °F	280 °F	−320 °F
E, lb/in^2	29.1×10^6	28.05×10^6	30.05×10^6
G, lb/in^2	10.4×10^6	10.04×10^6	10.6×10^6
ν	0.302	0.31	0.285
α, in/in-°F	9.17×10^{-6}	9.17×10^{-6}	$9.17 \times 10^{-6*}$
ρ, lb/in^3	0.287	0.287	0.287

[*]Actual data not available.

Table 4. Effective material properties of honeycomb core (age-hardened steel).

E_{11}	$= 0.1 \times 10^4$ lb/in^2
E_{22}	$= 0.1 \times 10^3$ lb/in^2
E_{33}	$= 0.1 \times 10^3$ lb/in^2
G_{12}	$= 0.75 \times 10^5$ lb/in^2
G_{23}	$= 0.1 \times 10^3$ lb/in^2
G_{31}	$= 0.4 \times 10^5$ lb/in^2
α_1	$= \alpha_2 = \alpha_3 = 8.1 \times 10^{-6}$ in/in-°F
ρ_{hc}	$= 0.432 \times 10^{-2}$ lb/in^3

In table 4, the subscripts {1, 2, 3} denote the radial, tangential, and axial (longitudinal) directions. Data for the effective Poisson's ratios for the honeycomb core were not available at the time of analysis. The effective Poisson's ratios for the honeycomb core are usually negligibly small (on the order of 10^{-3} to 10^{-7}; ref. 2); therefore, they are assumed to be zero in the analysis.

The finite-element analysis computes the effective radial tensile stress σ_{eff} for the honeycomb core. This stress is then converted to the actual radial tensile stress σ_r (defined as open-mode stress) induced in the honeycomb core cell wall according to the following relationship:

$$\sigma_r = \sigma_{eff} \frac{A_c}{A_w} = \sigma_{eff} \frac{\rho}{\rho_{hc}} \tag{1}$$

where A_c and A_w are, respectively, the cross-sectional areas of the honeycomb cell and cell wall (normal to the honeycomb cell generatrix); ρ and ρ_{hc} are, respectively, the weight densities of the honeycomb core material and core structure.

RESULTS

This section presents the results of finite-element, open-mode analysis of curved honeycomb-core sandwich panels subjected to thermocryogenic bending, including panel deformations, core depth changes, open-mode stresses, and face-sheet stresses.

Panel Deformations

Figures 4 through 11 show the deformed shapes of the curved sandwich panels with different curvatures supported under different boundary conditions. The undeformed shapes are superimposed on the deformed shapes to show the relative positions of both. In all plots, the panel displacements are magnified for the sake of visualization. In the figures, values of radial displacement δ_o at the midspan of the middle surface of each sandwich panel is indicated. The sign of δ_o is defined as positive for upward (outward) displacement and negative for downward (inward) displacement. For $\theta = 15°$ only (fig. 9(a)), in

addition to the value of midspan radial displacement δ_o (no longer maximum), the maximum radial displacements at two outer-span points are shown.

For the simply supported panels with curvature angles varying from $\theta = 90°$ to $\theta = 15°$ (figs. 4(a) through 9(a)), the midspan regions of the sandwich panels move inwardly (δ_o = negative), and the outer span regions bulge out. At $\theta = 45°$, 30°, 15° (figs. 7(a) through 9(a)), the panel deforms into shallow M shapes. For curvature angles $\theta = 5°$ and $\theta = 0°$, (figs. 10(a), 11(a)), the panel bows upward deforming into arch shapes without cave-in regions. The causes of M-shaped and arch-shaped deformations will be discussed later in the section, "Face Sheet Stresses." For the simply supported curved panels, the core depth stretching Δh (i.e., pulling apart of two face sheets) is maximum at the midspan, and gradually tapers down in tangential direction, and becomes zero at the panel supported edges because of constraint.

For the clamped panels, the midspan radial δ_o is positive at $\theta = 90°$ (fig. 4(b)) and then becomes negative as the curvature angle decreases (figs. 5(b) through 11(b)). At a curvature angle of $\theta = 5°$ (fig. 10(b)), the midspan region appears cave-in because of the magnified displacement plot. When the panel is flat, $\theta = 0°$, (fig. 11(b)), the midspan downward displacement becomes infinitesimal. For the clamped curved panels (figs. 4(b) through 10(b)), the core depth stretching appears almost uniform over the entire span (except for the supported panel edges). As will be shown shortly, the core depth stretching Δh becomes maximum at the midspan or at the outer spans depending on the value of curvature angle θ.

Figure 12 shows radial displacements δ_o at the midspan of the middle surface of the curved sandwich panel plotted as functions of curvature angle θ for the two different boundary conditions. The simply supported case induced markedly larger magnitude of midspan displacements δ_o (a maximum of 1,357 times larger at $\theta = 0°$) than the clamped case. For the simply supported case, the downward displacement of the midspan (δ_o = negative) is maximum at $\theta = 90°$, decreases monotonically with decreasing θ, turns to upward displacement (δ_o = positive) at approximately $\theta = 14°$, and finally increases steeply as θ approaches zero (flat panel).

For the clamped case, the midspan displacement δ_o is slightly upward (δ_o = positive) at curvature angle $\theta = 90°$, and turns downward (δ_o = negative) at around $\theta = 85°$. The downward displacement continues to increase with decreasing θ, reaching a peak at about $\theta = 10°$, and then decreases to a very small negative value at $\theta = 0°$.

Core Depth Changes

Figure 13 shows the maximum sandwich core depth changes $(\Delta h)_{max}$ plotted as functions of the curvature angle θ for the two cases of boundary conditions. For the simply supported case, $(\Delta h)_{max}$ is always at the midspan of the curved sandwich panels (flat panel excluded). For the clamped case, however, $(\Delta h)_{max}$ is at the midspan only for the panels with low-curvature angles $45° > \theta > 5°$. For the high-curvature angles $90° > \theta > 45°$, the location of $(\Delta h)_{max}$ shifts to the outer spans (near the edges) of the panel.

The simply supported boundary condition induces higher values of $(\Delta h)_{max}$ (a maximum of 22 percent higher at $\theta = 45°$) than the clamped case. As the curvature angle θ decreases from $\theta = 90°$, values of $(\Delta h)_{max}$ increase slightly and reach their peak (indicated on the figures with downward arrows) at $\theta = 75°$ for both boundary conditions, and then gradually decrease to very small negative values (contraction) at $\theta = 0°$. When the panel becomes flat ($\theta = 0°$), no curvature effects can induce core stretching, and the sandwich core contracts slightly, because the cryogenic contraction of the sandwich

core depth overcomes the effect of its thermal expansion. Table 5 lists the numerical values of $(\Delta h)_{max}$ used in plotting figure 13.

Table 5. Maximum sandwich core depth changes $(\Delta h)_{max}$ for different curvature angles θ.

θ, deg		90	75	60	45	30	15	5	0
$(\Delta h)_{max}$, in.	Simply supported	0.08736	0.08949	0.08838	0.08198	0.06413	0.03497	0.00841	–0.00028
	Clamped	0.07203[*]	0.07383[*]	0.07267[*]	0.06629[*]	0.05320	0.03053	0.01042	–0.00028

[*]Located at outer span; all others are located at midspan.

Figure 14 shows the distribution of the sandwich core depth changes Δh (positive for stretching) for the simply supported case in the l-θ space, where l is defined in figure 1. The distribution surface of Δh forms a distorted dome shape, with the apex at the midspan of θ = 75° panel. The peak value of Δh is indicated with a downward arrow. For any curved sandwich panel, Δh is maximum at the panel midspan and gradually approaches zero toward the panel edge. The curve for connecting the midspan values of Δh ($= (\Delta h)_{max}$) for different θ is indicated in figure 14. This curve is identical to the $(\Delta h)_{max}$ curve for the simply supported case shown in figure 13. At θ = 0° (flat panel), the tangential distribution of Δh becomes flat with slightly negative values (contraction) over the entire span except for panel edges reflecting the overbalanced cooling of sandwich core as explained earlier.

Figure 15 shows the distribution of sandwich core depth changes Δh in the l-θ space for the clamped case. The distribution surface of Δh for the clamped case is cascade shaped with the apex (peak value of $\Delta h = (\Delta h)_{max}$) at the outer span of θ = 75° panel as indicated with a downward arrow. For high-curvature angles 90° > θ > 45°, the value of Δh tapers up slightly (almost linearly) from its midspan minimum value toward the outer span, reaching its peak before suddenly dropping to zero at the panel edges. For low-curvature angles 45° > θ > 5°, Δh is maximum at the midspan and decreases infinitesimally and practically linearly toward the outer span and then drops suddenly to zero at the panel edges because of edge constraints. The $(\Delta h)_{max}$ curve shown in figure 13 for the clamped case is actually a composite curve consisting of a segment of the curve at the outer span (curve with arrow sign attached) over the curvature angle range 90° > θ > 45° where $\Delta h = (\Delta h)_{max}$, and a segment of the curve at the midspan over the range 45° > θ > 5° where $\Delta h = (\Delta h)_{max}$ (fig. 15). When the panel is flat (θ = 0°), Δh becomes slightly negative (contraction) and is practically constant over the entire panel span (except for the panel edges) because of overbalanced cooling as mentioned earlier.

Open-Mode Stresses

Figures 16 through 21 show the tangential distributions of local maximum open-mode stresses $(\sigma_r)_d$ induced in the curved sandwich panels with different curvature angles θ. As will be seen later, $(\sigma_r)_d$ is at the inner bonding interface between the inner face sheet and the sandwich core.

For the simply supported case, the maximum open-mode stress $(\sigma_r)_d = (\sigma_r)_{max}$ is always at the midspan of the curved sandwich panel. The values of $(\sigma_r)_d$ decrease monotonically (convex downward) in the tangential direction from its midspan maximum values $(\sigma_r)_{max}$, and down to zero at the panel edges.

For the clamped cases shown in the figures with dashed curves, the tangential distribution of $(\sigma_r)_d$ remains almost constant over the span up to the panel edges where $(\sigma_r)_d$ drops rapidly to zero because of clamping. The maximum open-mode stress $(\sigma_r)_{max}$ is at the midspan of the panel of low-curvature angle; $45° > \theta > 5°$; and its location shifts to outer spans of the panel with high curvature angle $90° > \theta > 45°$.

Figure 22 shows the plots of maximum open-mode stresses $(\sigma_r)_{max}$ as functions of the curvature angle θ for the two cases of boundary conditions. For the simply supported case, $(\sigma_r)_{max}$ is at the midspan of the inner bonding interface. For the clamped case (similar to $(\Delta h)_{max}$ in figure 13), however, $(\sigma_r)_{max}$ is at the midspan of the inner bonding interface for the curvature range $45° > \theta > 5°$, or at the outer spans of the inner bonding interface for the curvature angle range $90° > \theta > 45°$. The simply supported case induces higher values of $(\sigma_r)_{max}$ than the clamped case, with a maximum of 32 percent higher at $\theta = 90°$. The peak values of $(\sigma_r)_{max}$ occur at $\theta = 75°$ for both boundary conditions. The shapes of the $(\sigma_r)_{max}$ curves and the locations of peak values directly reflect characteristics of the $(\Delta h)_{max}$ curves shown in figure 13. Table 6 lists the numerical values of $(\sigma_r)_{max}$ used in plotting figure 22.

Table 6. Maximum open-mode stress $(\sigma_r)_{max}$ for different curvature angles θ.

θ, deg		90	75	60	45	30	15	5	0
$(\sigma_r)_{max}$, lb/in^2	Simply supported	4,434	4,533	4,480	4,134	3,330	1,940	611	0
	Clamped	3,550[*]	3,619[*]	3,544[*]	3,220[*]	2,574	1,489	530	0

[*]Located at outer span; all others are located at midspan.

Figure 23 shows the distribution of the local maximum open-mode stresses $(\sigma_r)_d$ in the l-θ space for the simply supported case. The distribution of $(\sigma_r)_d$, like that of Δh (fig. 14), also forms a distorted dome shape, with its apex (peak value of $(\sigma_r)_d = (\sigma_r)_{max}$) indicated with a downward arrow, at the midspan of the $\theta = 75°$ panel. For any curvature angle θ, the values of $(\sigma_r)_d$ reach their peak $(\sigma_r)_d = (\sigma_r)_{max}$ at the midspan, and gradually taper down to zero toward the panel edge. The curve for connecting the midspan values $(\sigma_r)_{max}$ is indicated in the figure. This curve is identical to the $(\sigma_r)_{max}$ curve for the simply supported case shown earlier in figure 22. At $\theta = 0°$ (flat), $(\sigma_r)_d$ is zero over the span.

Figure 24 shows the local maximum open-mode stresses $(\sigma_r)_d$ plotted in the l-θ space for the clamped case. The surface of $(\sigma_r)_d$ distribution for the clamped case looks similar to a cascade, with its apex (peak value of $(\sigma_r)_d = (\sigma_r)_{max}$) at the outer span of $\theta = 75°$ panel (indicated on figure with a downward arrow). For any curvature angle θ, the value of $(\sigma_r)_d$ appears almost constant over the panel span, and then suddenly drops to zero at the panel edge. When the panel is flat ($\theta = 0°$), $(\sigma_r)_d$ is zero everywhere. The segment of curve at the outer span (curve with vertical arrow sign attached) over the

curvature angle range $90° > \theta > 45°$ where $(\sigma_r)_d = (\sigma_r)_{max}$ and the segment of curve at the midspan over the range $45° > \theta > 5°$ where $(\sigma_r)_d = (\sigma_r)_{max}$ form the composite $(\sigma_r)_{max}$ curve for the clamped case shown earlier in figure 22.

Figures 25 and 26, respectively, show the radial distributions of open-mode stress σ_r along the y-axis (i.e., along the midspan core depth direction) for the simply supported and the clamped boundary conditions. For both types of boundary conditions, the radial distribution of σ_r for any curvature angle θ ($\theta \neq 0°$) is almost linear, and tapers down very little toward the outer bonding interface. For the flat panel ($\theta = 0°$), σ_r is zero everywhere in the core.

For the simply supported case (fig. 25), $\sigma_r = (\sigma_r)_{max}$ is at the inner bonding interface (between the inner face sheet and the sandwich core), and the curve indicated in the figure is identical to the $(\sigma_r)_{max}$ curve shown earlier in figure 22 for the simply supported case.

For the clamped case (fig. 26), the segment of $(\sigma_r)_{max}$ curve lying in the region $\theta < 45°$ is the midspan $(\sigma_r)_{max}$ curve segment shown earlier in figure 22 for the clamped case.

Face-Sheet Stresses

Figures 27 through 34 show the tangential distributions of tangential stresses $\{\sigma_\theta^l, \sigma_\theta^u\}$ induced in the concave (lower) and convex (upper) face sheets for different curvature angles θ for the simply supported case. The plus (+) and minus (–) signs alongside the $\{\sigma_\theta^l, \sigma_\theta^u\}$ curves imply tension and compression, respectively. The concave face sheet is under tension (σ_θ^l = positive) because of restrained cryogenic contraction, and the convex face sheet (except for the panel edge regions, figs. 29 through 33) is under compression (σ_θ^u = negative) because of restrained thermal expansion. For a given curvature angle θ, the magnitude of σ_θ^l is always larger than that of σ_θ^u because of panel curvature and the unequal thermo-cryogenic loading condition. As θ decreases from $\theta = 90°$, the difference between the magnitudes of $\{\sigma_\theta^l, \sigma_\theta^u\}$ grows larger (figs. 27 through 33), and then becomes practically zero at $\theta = 0°$ (fig. 34). Also, as θ decreases, σ_θ^u in the convex face sheet near the panel edges begins to grow from negative to positive (figs. 29 through 33) because of the load transfer from the concave face sheet through the edge rigid rods. These panel edge tensile zones in the convex face sheet continue to grow larger as θ becomes smaller, and finally extend to the entire panel span at $\theta = 0°$ (fig. 34).

The tangential stresses of opposite signs induced in the two face sheets (figs. 27 through 33) generate thermal moments $[= (\sigma_\theta^l - \sigma_\theta^u)h/2]$ that tend to bend the curved panels downward, thus appearing to be caved in. For a given curvature angle θ, the cave-in thermal moments reach maximum intensity at the midspan and gradually taper down toward the panel edges. At $\theta = 0°$ (flat panel, fig. 34), the cave-in thermal moments diminish because both $\{\sigma_\theta^l, \sigma_\theta^u\}$ have practically identical small positive values that are constant over the entire panel span.

Figure 35 shows the midspan magnitudes of $\{\sigma_\theta^l, \sigma_\theta^u\}$ plotted as functions of curvature angle θ for the simply supported case. The stress magnitude $(\sigma_\theta^l - \sigma_\theta^u)/2$ of the cave-in thermal moments $[= (\sigma_\theta^l - \sigma_\theta^u)h/2]$ is also plotted. The value of $(\sigma_\theta^l - \sigma_\theta^u)/2$ increases as θ decreases from $\theta = 90°$,

reaching a maximum at $\theta = 15°$ where the M-shaped deformation is the most pronounced (fig.9(a)), and then decreases rapidly toward zero at $\theta = 0°$. At $\theta = 3°$, σ_θ^u changes sign from negative to positive and then reaches a small positive value practically identical to the value of σ_θ^l (fig. 34) as θ approaches $\theta = 0°$.

Figure 36 shows the causes of the shallow M-shaped deformation of a typical $\theta = 15°$, (fig. 9(a)) simply supported curved panel. Because of the cryogenic contraction of the concave face sheet and the thermal expansion of the convex face sheet, the simply supported panel edges are forced to rotate about the fixed support points, causing upward bowing of the panel. Simultaneously, the induced cave-in thermal moments (maximum at the midspan) try to bend the panel downward, resulting in the M-shaped deformation. At lower curvature angles (e.g., $\theta = 5°$), the upward bowing effect begins to overshadow the cave-in bending effect, causing the curved panel to deform into a shallow arch shape (fig. 10(a)). The transition from M-shaped to arch-shaped deformation occurs in the neighborhood of $\theta = 7°$ for the present study.

Figures 37 through 39 show the tangential distributions of tangential stresses $\{\sigma_\theta^l, \sigma_\theta^u\}$ induced in the concave and convex face sheets for different curvature angles θ for the clamped case. The distributions of $\{\sigma_\theta^l, \sigma_\theta^u\}$ [or the cave-in thermal moments $= (\sigma_\theta^l - \sigma_\theta^u)h/2$] are almost constant over the panel span for the larger curvature angles between $\theta = 90°$ and $\theta = 30°$ (fig. 37), and starts to taper down slightly toward the panel edges at smaller curvature angles $\theta = 15°$ to $\theta = 5°$ (figs. 37 and 38). The differences in the magnitudes of $\{\sigma_\theta^l, \sigma_\theta^u\}$ are almost inconspicuous for $\theta = 90°$ to $\theta = 30°$ panels, and start to grow larger with decreasing curvature angle θ. At $\theta = 0°$ (fig. 39), the magnitudes of both $\{\sigma_\theta^l, \sigma_\theta^u\}$ are constant everywhere over the panel span (i.e., constant cave-in thermal moments, fig. 11(b)).

Figure 40 shows the midspan magnitudes of $\{\sigma_\theta^l, \sigma_\theta^u\}$ plotted as functions of curvature angle θ for the clamped case. The stress magnitude $(\sigma_\theta^l - \sigma_\theta^u)/2$ for the cave-in thermal moment $[= (\sigma_\theta^l - \sigma_\theta^u)h/2]$ is also plotted. The value of $(\sigma_\theta^l - \sigma_\theta^u)/2$ increases as θ decreases from $\theta = 90°$, reaching a maximum at $\theta = 5°$ where the most pronounced cave-in deformation occurs, (fig.10(b)), and then decreases slightly as θ approaches $\theta = 0°$.

Figure 41 shows the causes of cave-in deformation of a typical clamped panel ($\theta = 5°$). Because of the clamped edges without rotations, upward bowing effect is constrained, and the cave-in thermal moments (almost constant over the entire panel span) bend the panel downward into the cave-in shape.

DISCUSSION

The near-linear radial distribution of σ_r across the core depth is typical for the curved honeycomb-core sandwich panels, and was observed also in horseshoe- and elliptic-curved honeycomb-core sandwich bars subjected to open-mode mechanical bending (ref. 15). For a classical solid curved beam on the other hand, the radial distribution of σ_r at any tangential cross-section is arch shaped, with zero values at the inner and the outer boundaries, and the local maximum value at a point slightly inward of the middle surface of the curved beam (refs. 7 through 15).

For the present cases of curved sandwich panels ($\theta \neq 0°$) under thermocryogenic loading, the inner bonding interface at the midspan or at the outer spans is, therefore, the potential debonding failure initiation region. The deformed shapes of curved sandwich panels presented (figs. 4 through 11) show that

the midspan and outer spans of the curved sandwich panels are the critical high deflection points. Thus, in using the curved sandwich panels as reinforcing structures operating under thermocryogenic environment, those critical high deflection points must be properly constrained (in addition to the panel edges) to preserve the original shapes. Because the clamped boundary condition induces smaller panel deflections and lower levels of open-mode stress field, by supporting the curved panel edges as close as the theoretical clamped condition, concerns of excess panel deflections and of the open-mode debonding failure could be minimized.

CONCLUSIONS

Finite-element open-mode debonding analysis was performed on a family of curved honeycomb-core sandwich panels subjected to thermocryogenic bending. The effects of panel curvature and boundary condition on the open-mode stress distributions and the deformation fields were studied in detail. The key findings may be summarized in the following:

1. The peak panel deflection occurs at the midspan of the curved sandwich panel under both simply supported and clamped boundary conditions (exception: simply supported curved panel with curvature angle $\theta = 15°$, for which the peak panel deflections occur at outer spans).

2. The radial distribution of open-mode stress in the core of a curved sandwich panel is practically linear, with local maximum and minimum values located, respectively, at the inner and outer bonding interfaces. The minimum value is only slightly lower than the maximum value.

3. For a simply supported curved sandwich panel, the maximum open-mode stress point (or maximum core stretching point—the potential debonding failure initiation point) is always at the midspan of the inner bonding interface.

4. For the clamped case, the maximum open-mode stress point (or maximum core stretching point) is at the midspan of the inner bonding interface for low-curvature panels only, and shifts to the outer spans of the inner bonding interface for high-curvature panels.

5. The magnitude of the maximum open-mode stress (or maximum sandwich core stretching) increases with increasing panel curvature, reaching maximum at curvatures angle $\theta = 75°$, and then decreases slightly as the panel turns to a quarter circle ($\theta = 90°$) under both simply supported and clamped boundary conditions.

6. In general, clamping a curved sandwich panel induces smaller panel deflections, lower open-mode stresses, and less core depth stretching than simply supporting the panel.

Dryden Flight Research Center
National Aeronautics and Space Administration
Edwards, California, February 3, 1999

REFERENCES

1. Rhodes, Tom, "History of the Airframe, Part III," *Aerospace Engineering*, Sept. 1989, pp. 27–32.

2. Simons, Graham M., "Mosquito: The Original Multi-Role Aircraft," *Arms and Armor*, London, 1990.

3. Bishop, Edward, "Mosquito: The Wooden Wonder," Smithsonian Institute Press, Washington, D. C., 1990.

4. Hardy, Michael John, "The de Havilland Mosquito," Arco Pub. Co., 1977.

5. Ko, William L., Robert D. Quinn, and Leslie Gong, *Finite-Element Reentry Heat Transfer Analysis of Space Shuttle Orbiter*, NASA TP-2657, Dec. 1996.

6. Ko, William L., *Thermostructural Behavior of a Hypersonic Aircraft Sandwich Panel Subjected to Heating on One Side*, NASA TM-4769, April 1997.

7. Kedward, K. T., R. S. Wilson and S. K. McLean, "The Flexure of Simply Curved Composite Shapes," *Composites*, vol. 20, no. 6, Nov. 1989, pp. 527–536.

8. Jackson, Wade C. and Roderick H. Martin, *An Interlaminar Tension Strength Specimen*, NASA TM-107623, May 1992.

9. Martin, R. H. and W. C. Jackson, *Damage Prediction in Cross-Plied Curved Composite Materials*, NASA TM-104089, July 1991.

10. Hiel, Clement C., Mark Sumich and David P. Chappell, "A Curved Beam Test Specimen for Determining the Interlaminar Tensile Strength of a Laminated Composite," *J. Composite Materials*, vol. 25, July 1991, pp. 854–868.

11. Mao, T. H. and M. J. Owen, "Through-the-Thickness Tensile Strength of Fiber-Reinforced Plastics," *Composite Materials: Testing and Design (Sixth Conference)*, ASTM STP 787, American Society for Testing Materials, 1982, pp. 5–18.

12. Lagace, P. A. and D. B. Weems, "A Through-the-Thickness Strength Specimen for Composites," presented at the second ASTM Symposium on Test Methods and Design Allowables, Phoenix, Arizona, 1986.

13. Ige, D. and P. Sargent, "An Apparatus for Determining the Interlaminar Tensile Strength of Laminated Composites Using the Curved Specimen Geometry," presented at the European Conference on Composites Testing and Standardisation, Amsterdam, The Netherlands, Sept. 8–10, 1992.

14. Ko, William L. and Raymond H. Jackson, *Multilayer Theory for Delamination Analysis of a Composite Curved Bar Subjected to End Forces and End Moments,* NASA TM-4139, Sept. 1989.

15. Ko, William L., *Delamination Stresses in Semicircular Laminated Composite Bars*, NASA TM-4026, Jan. 1988.

16. Ko, William L. and Raymond H. Jackson, *Open-Mode Delamination Stress Concentrations in Horseshoe and Elliptic Composite Curved Bars Subjected to End Forces*, NASA TM-4164, Jan. 1990.

17. Whetstone, W. D., *SPAR Structural Analysis System Reference Manual, System Level 13A, vol. 1, Program Execution*, NASA CR-158970-1, Dec. 1978.
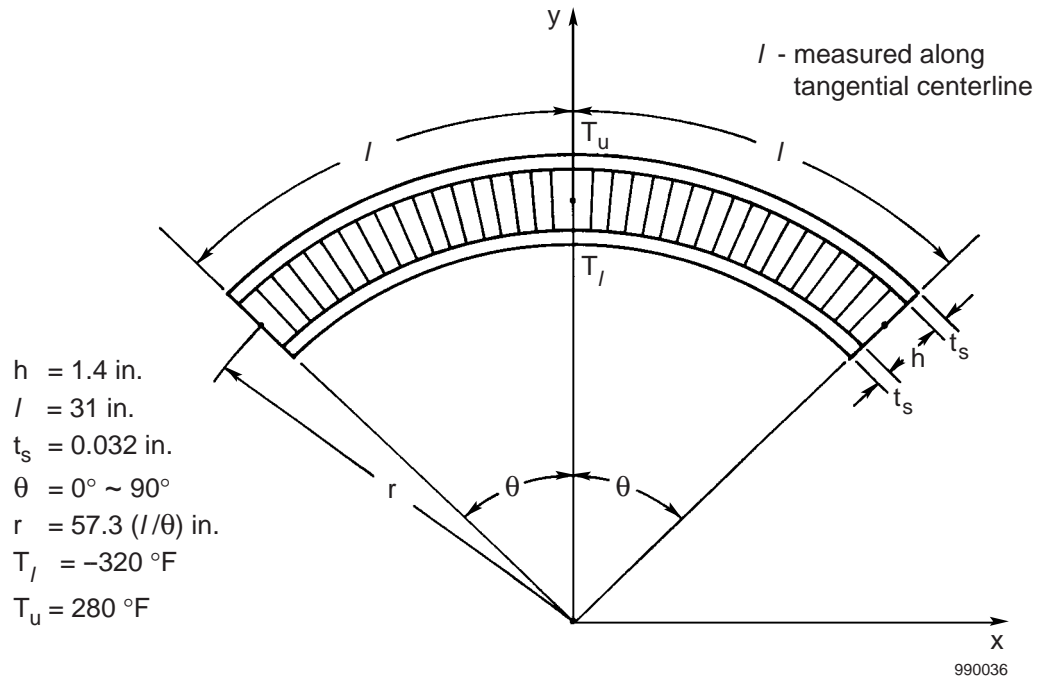
Figure 1. Curved honeycomb-core sandwich panel subjected to heating and cryogenic cooling on opposite sides.

$h = 1.4$ in.
$l = 31$ in.
$t_s = 0.032$ in.
$\theta = 0° \sim 90°$
$r = 57.3 (l/\theta)$ in.
$T_l = -320$ °F
$T_u = 280$ °F

(a) Simply supported.
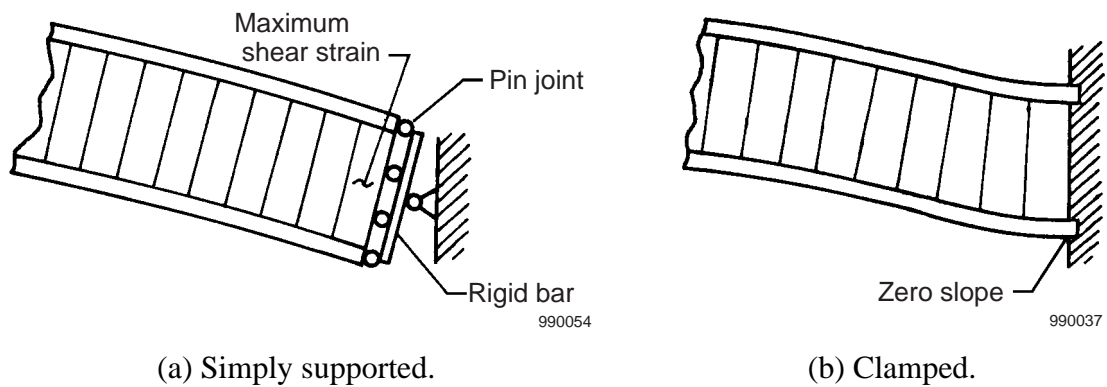
(b) Clamped.

Figure 2. Two types of edge support conditions for the sandwich panel.

15

JLOC   2211
E41 elements   1600
E43 elements   400

θ = 90°

y

x

990038
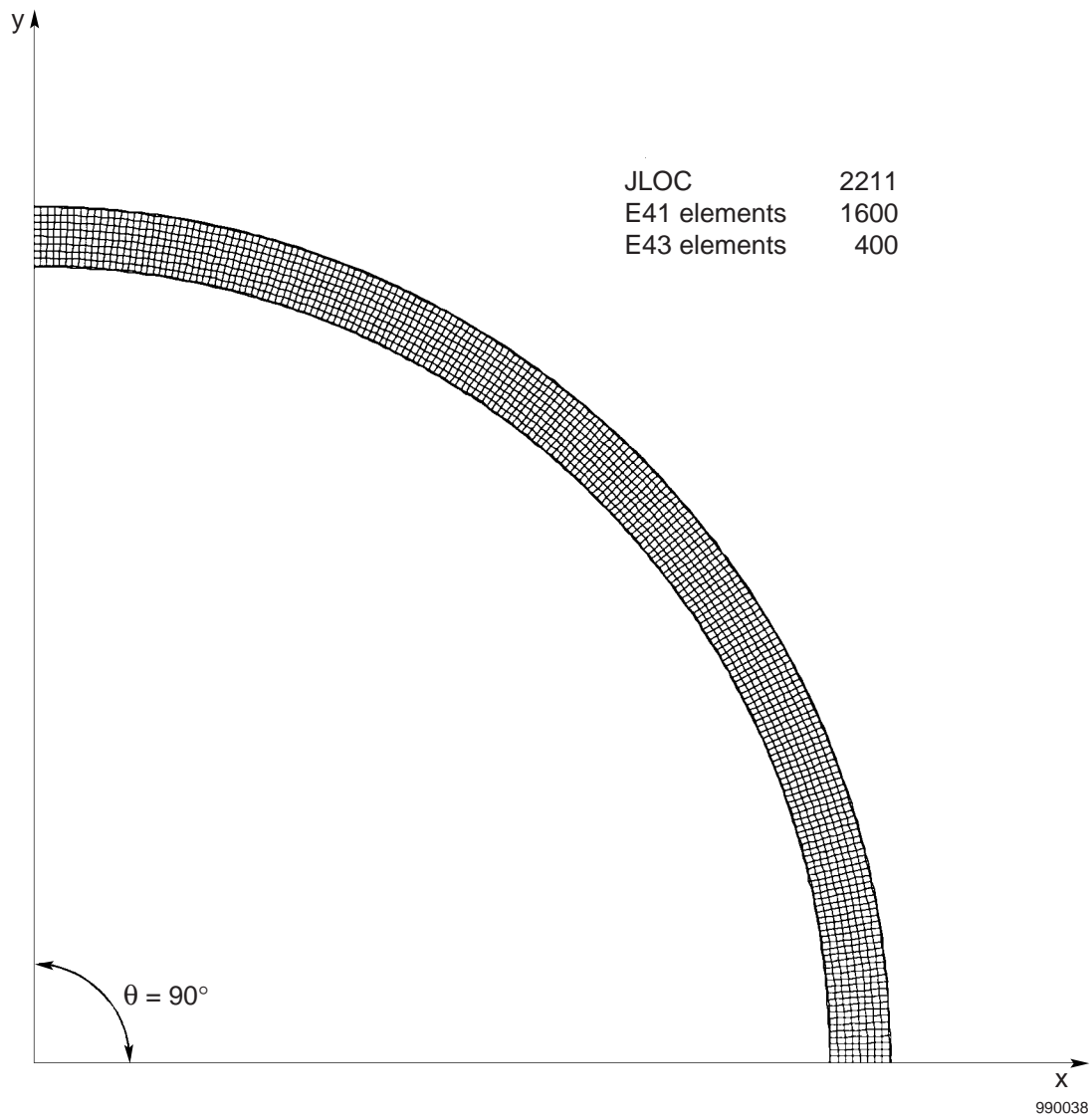
Figure 3. Semi-span finite-element model for the curved honeycomb-core sandwich panel; θ = 90°.
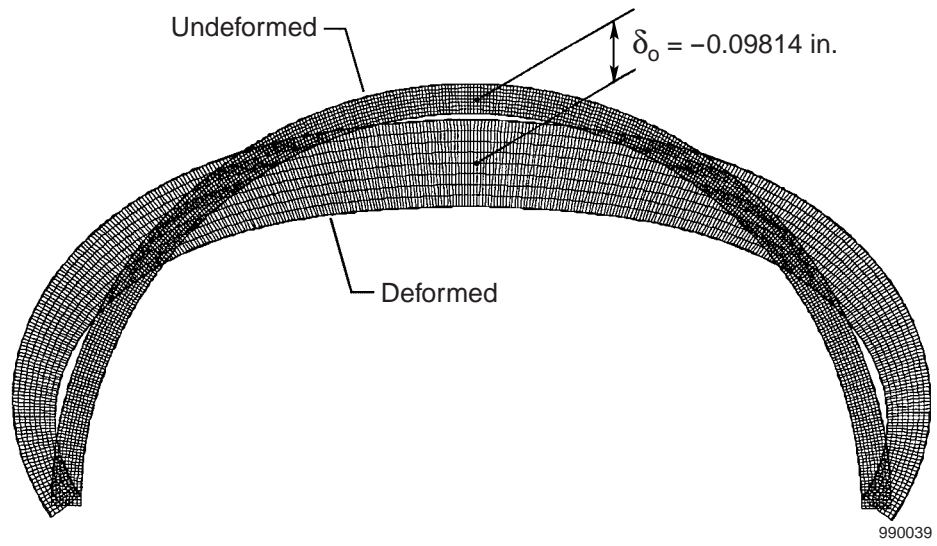
(a) Simply supported.
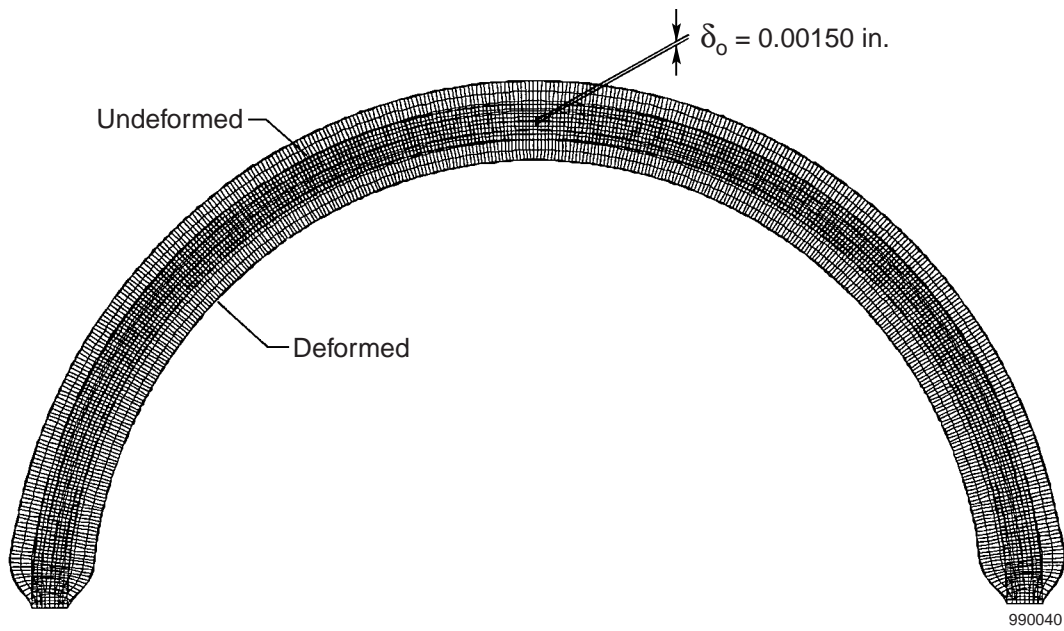
(b) Clamped.

Figure 4. Deformed shapes of curved honeycomb-core sandwich panel; $T_u = 280$ °F; $T_l = -320$ °F; $\theta = 90°$.

17
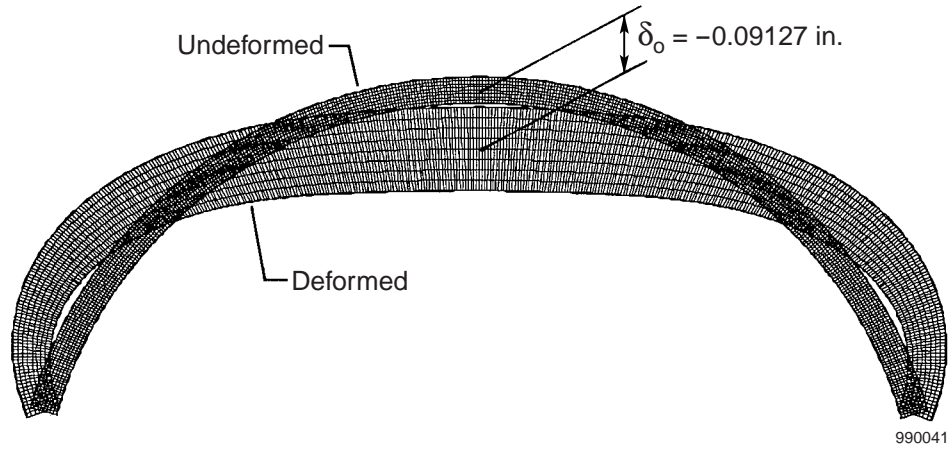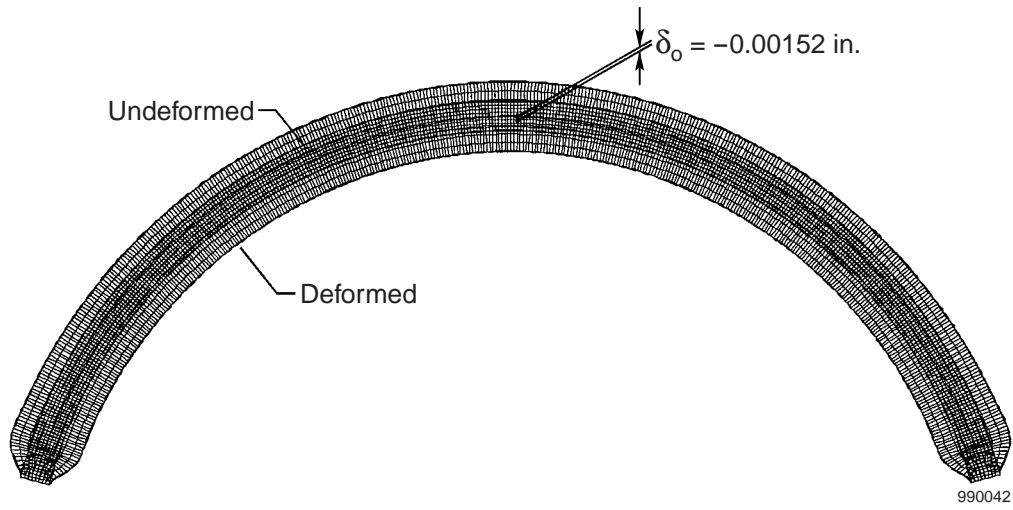
(a) Simply supported.

(b) Clamped.

Figure 5. Deformed shapes of curved honeycomb-core sandwich panel; $T_u = 280\ °\text{F}$; $T_l = -320\ °\text{F}$; $\theta = 75°$.
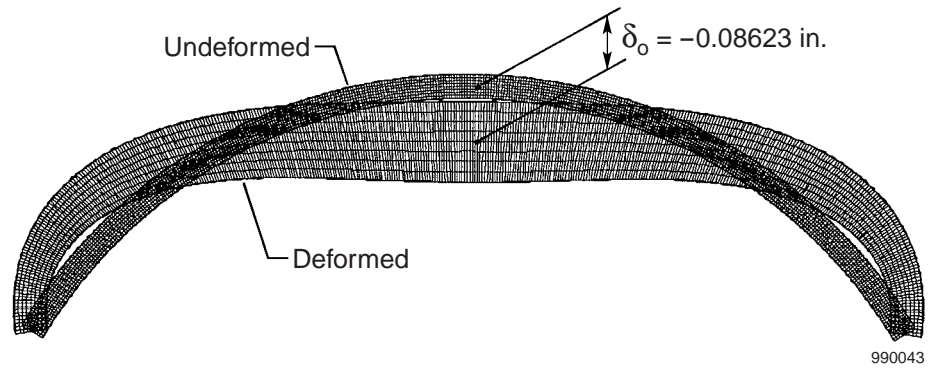
(a) Simply supported.
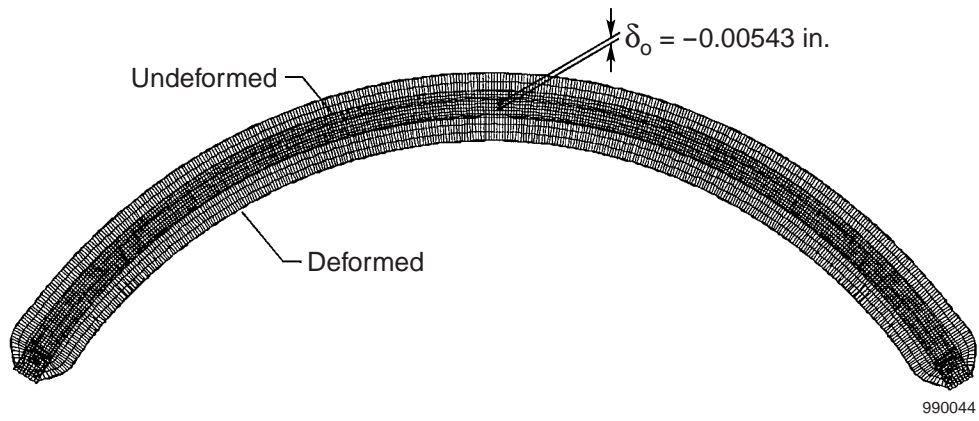
(b) Clamped.

Figure 6. Deformed shapes of curved honeycomb-core sandwich panel; $T_u = 280$ °F; $T_l = -320$ °F; $\theta = 60°$.
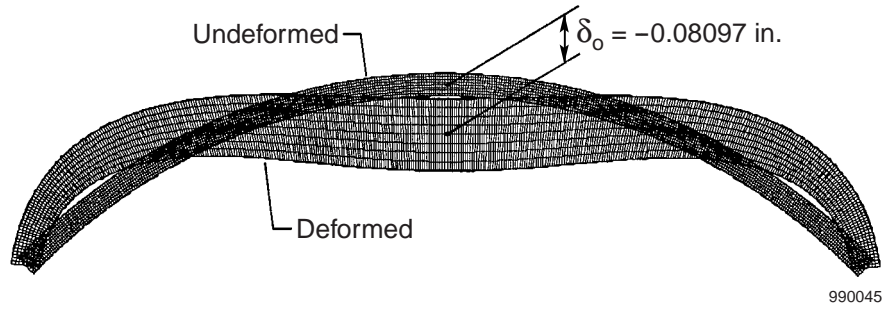
(a) Simply supported.
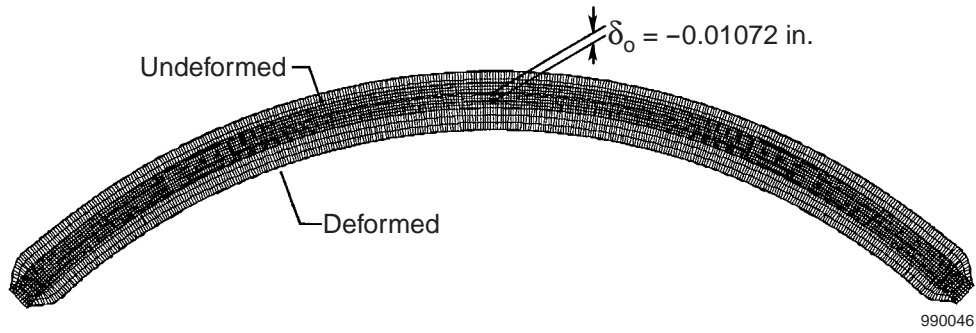
(b) Clamped.

Figure 7. Deformed shapes of curved honeycomb-core sandwich panel; $T_u = 280\ °\text{F}$; $T_l = -320\ °\text{F}$; $\theta = 45°$.
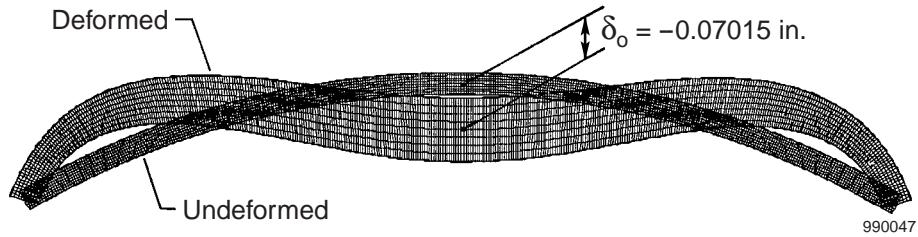
(a) Simply supported.
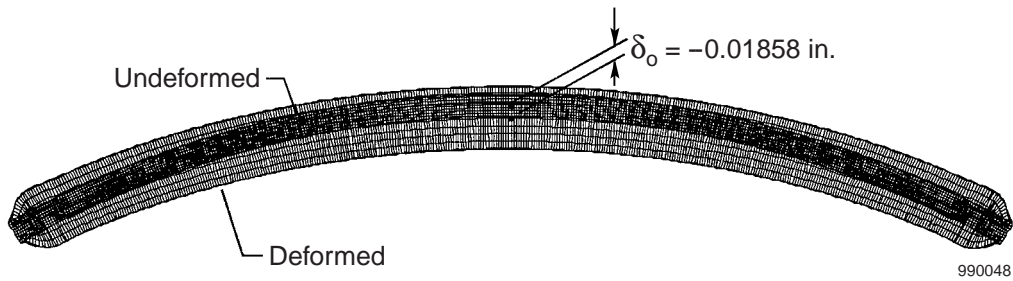
(b) Clamped.

Figure 8. Deformed shapes of curved honeycomb-core sandwich panel; $T_u = 280\ °\text{F}$; $T_l = -320\ °\text{F}$; $\theta = 30°$.

$\delta_o = -0.00788$ in.

Deformed

0.08749 in.

Undeformed

990049

(a) Simply supported.

Undeformed

$\delta_o = -0.03212$ in.

Deformed

990050
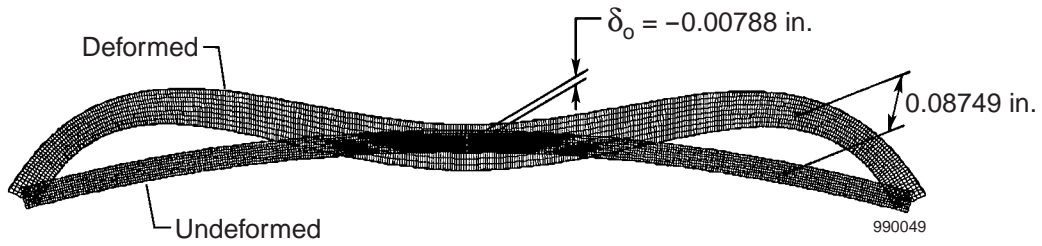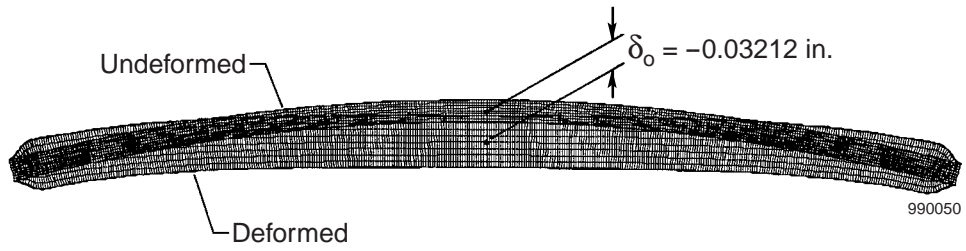
(b) Clamped.

Figure 9. Deformed shapes of curved honeycomb-core sandwich panel; $T_u = 280$ °F; $T_l = -320$ °F; $\theta = 15°$.

Deformed

$\delta_o = 0.50800$ in.

Undeformed

990051

(a) Simply supported.

Undeformed

$\delta_o = -0.03327$ in.

Deformed

990052
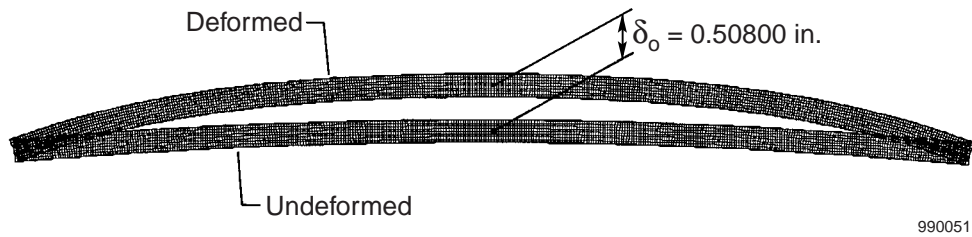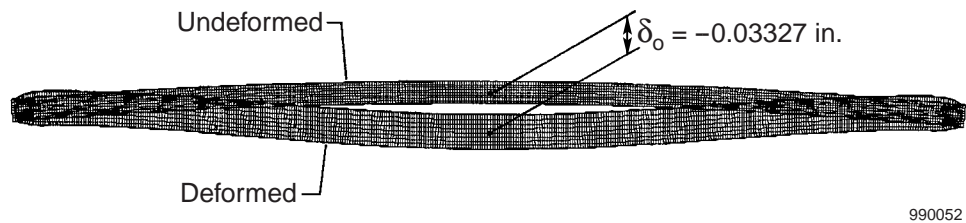
(b) Clamped.

Figure 10. Deformed shapes of curved honeycomb-core sandwich panel; $T_u = 280$ °F; $T_l = -320$ °F; $\theta = 5°$.

21
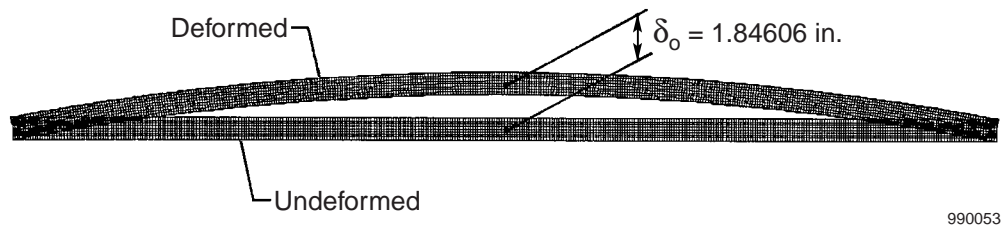
(a) Simply supported.
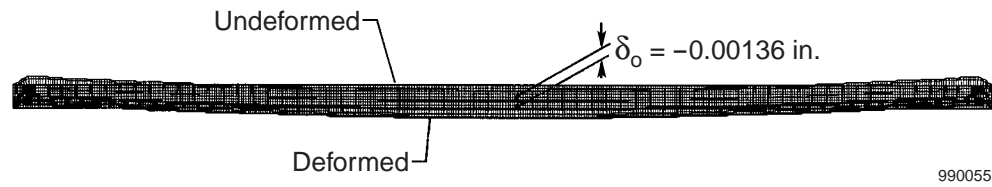
(b) Clamped.

Figure 11. Deformed shapes of curved honeycomb-core sandwich panel; $T_u = 280$ °F; $T_l = -320$ °F; $\theta = 0°$ (flat).
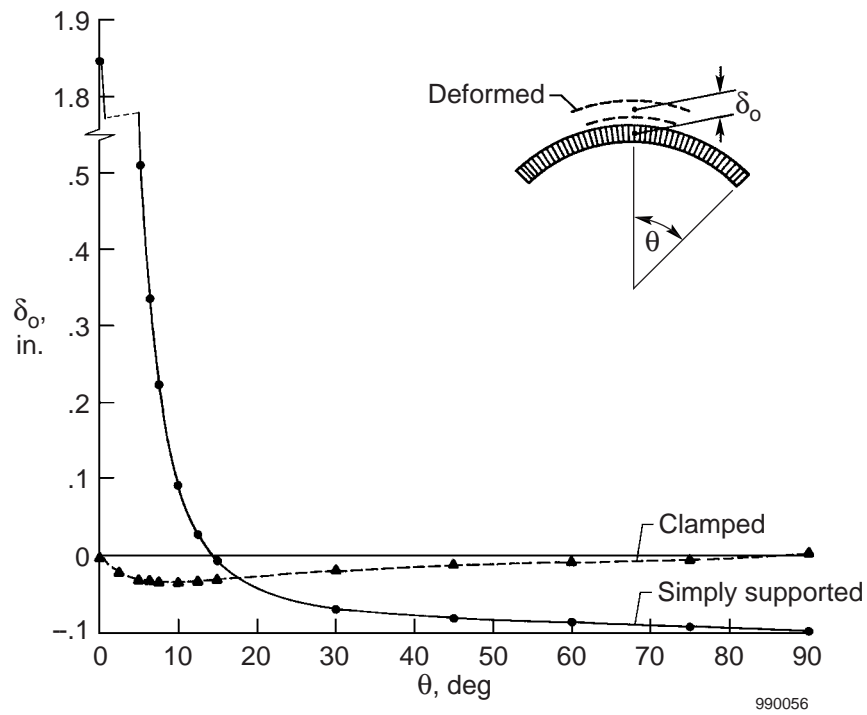
Figure 12. Plots of radial displacements δ_o (positive upward) at midspan of curved sandwich panel as functions of curvature angle θ; $T_u = 280$ °F; $T_l = -320$ °F.
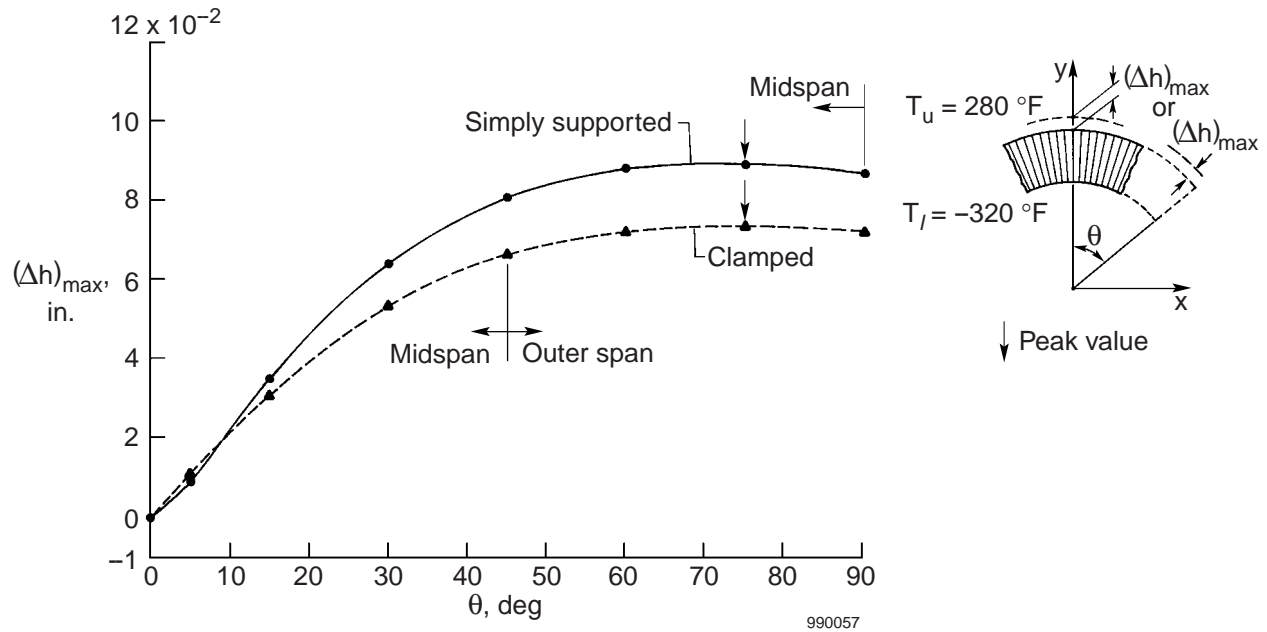
Figure 13. Plots of honeycomb core maximum depth changes $(\Delta h)_{max}$ (at midspan or outer span, positive for stretching) of curved sandwich panel as functions of curvature angle θ; $T_u = 280\ °F$; $T_l = -320\ °F$.
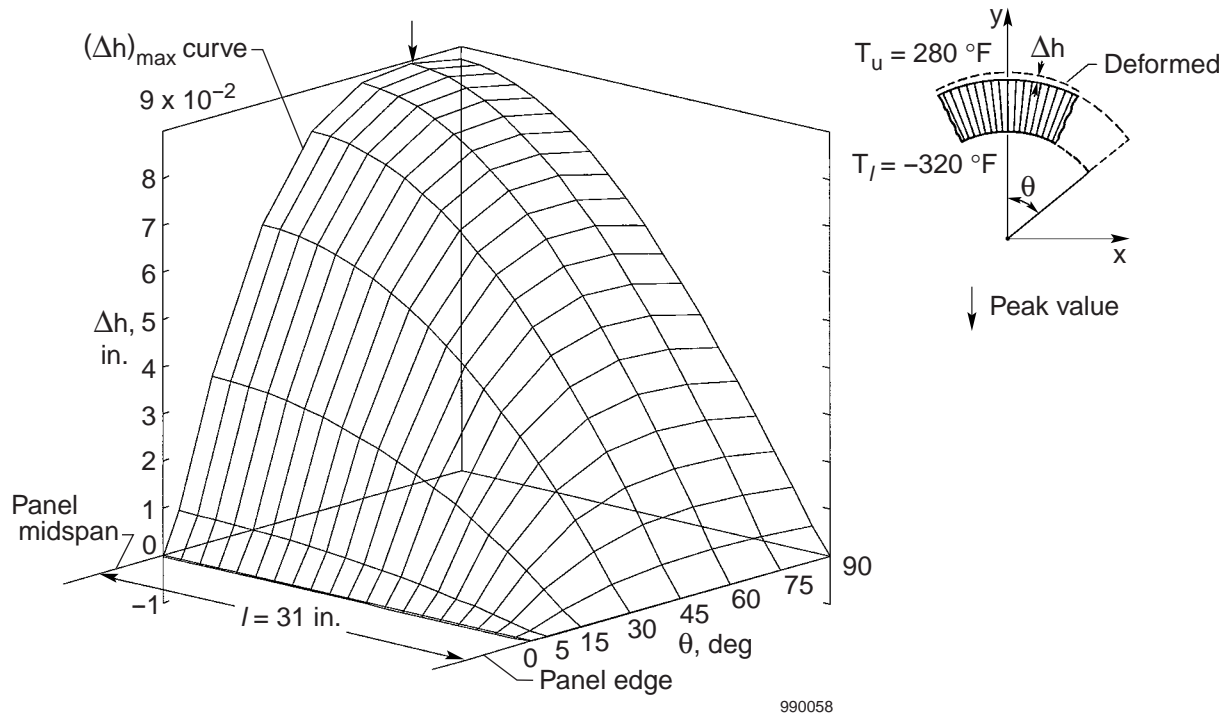
Figure 14. Distributions of honeycomb core depth change Δh (positive for stretching) in the l-θ space; $T_u = 280\ °F$; $T_l = -320\ °F$; simply supported.

23
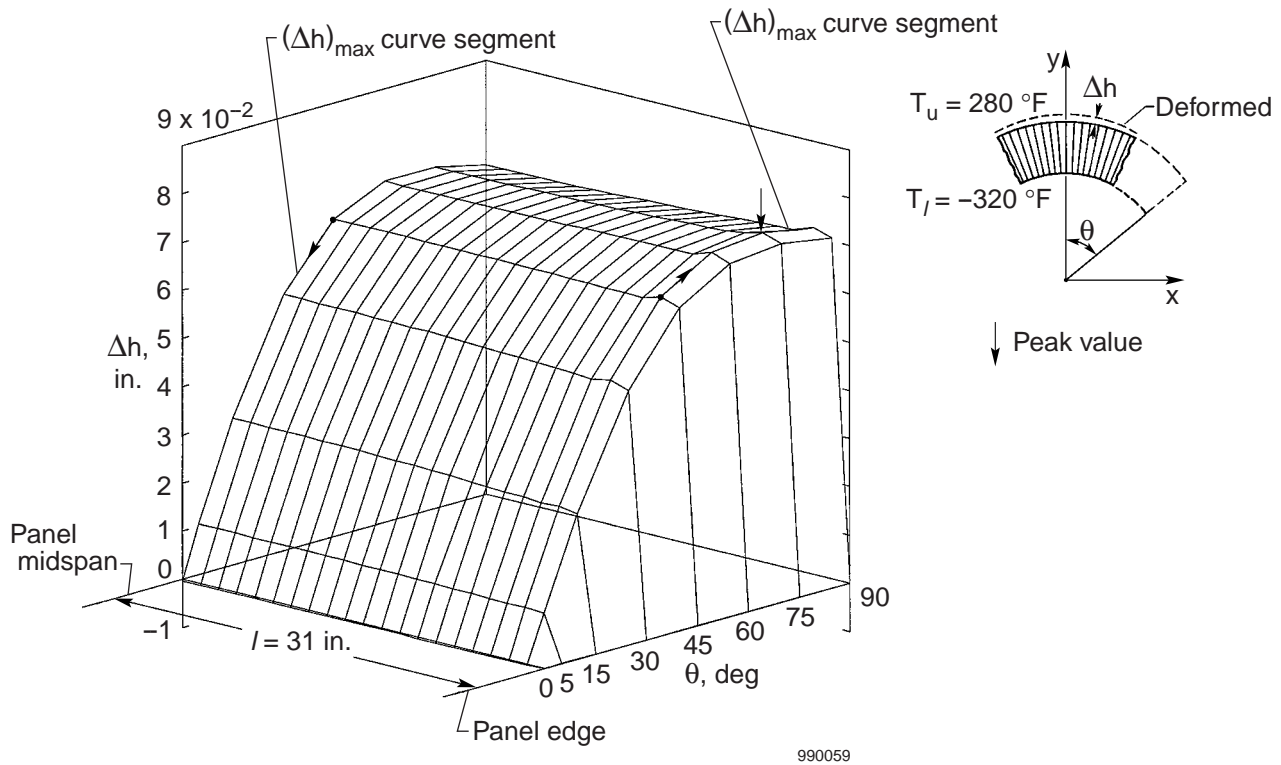
Figure 15. Distributions of honeycomb core depth change Δh (positive for stretching) in the l-θ space; $T_u = 280$ °F; $T_l = -320$ °F; clamped.
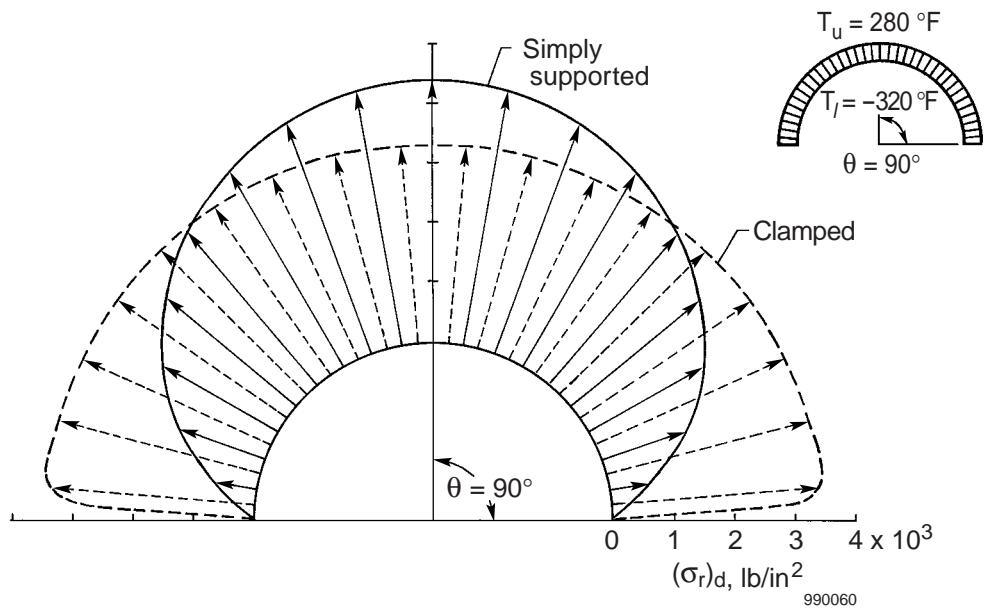
Figure 16. Tangential distributions of local maximum open-mode stress $(\sigma_r)_d$ in curved honeycomb core; $T_u = 280$ °F; $T_l = -320$ °F; $\theta = 90°$.

Figure 17. Tangential distributions of local maximum open-mode stress $(\sigma_r)_d$ in curved honeycomb core; $T_u = 280$ °F; $T_l = -320$ °F; $\theta = 75°$.

Figure 18. Tangential distributions of local maximum open-mode stress $(\sigma_r)_d$ in curved honeycomb core; $T_u = 280$ °F; $T_l = -320$ °F; $\theta = 60°$.
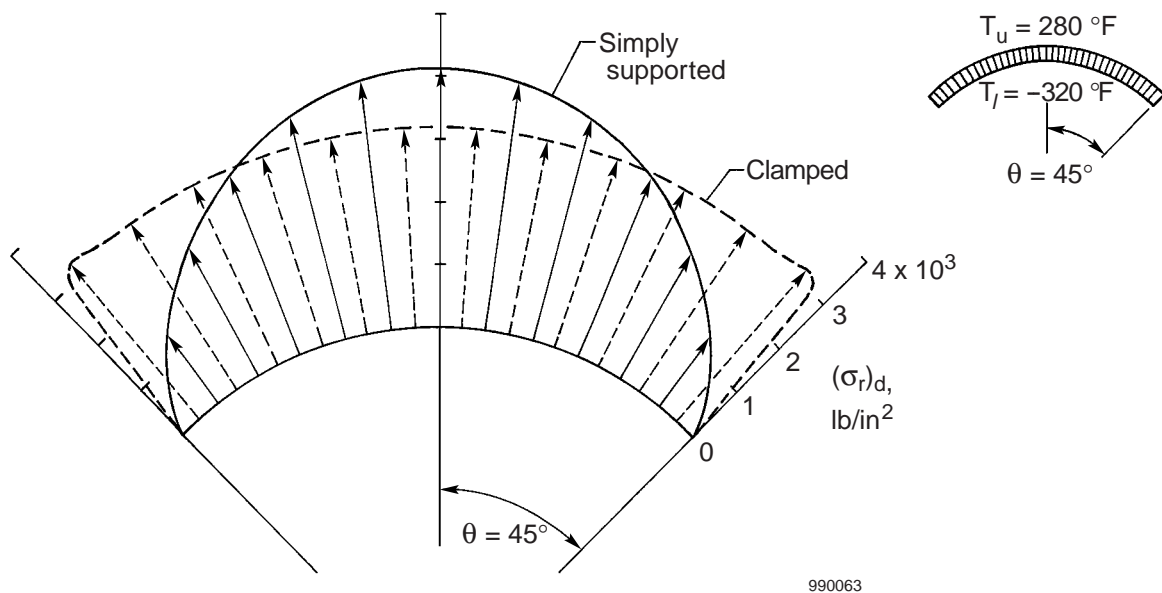
Figure 19. Tangential distributions of local maximum open-mode stress $(\sigma_r)_d$ in curved honeycomb core; $T_u = 280$ °F; $T_l = -320$ °F; $\theta = 45°$.
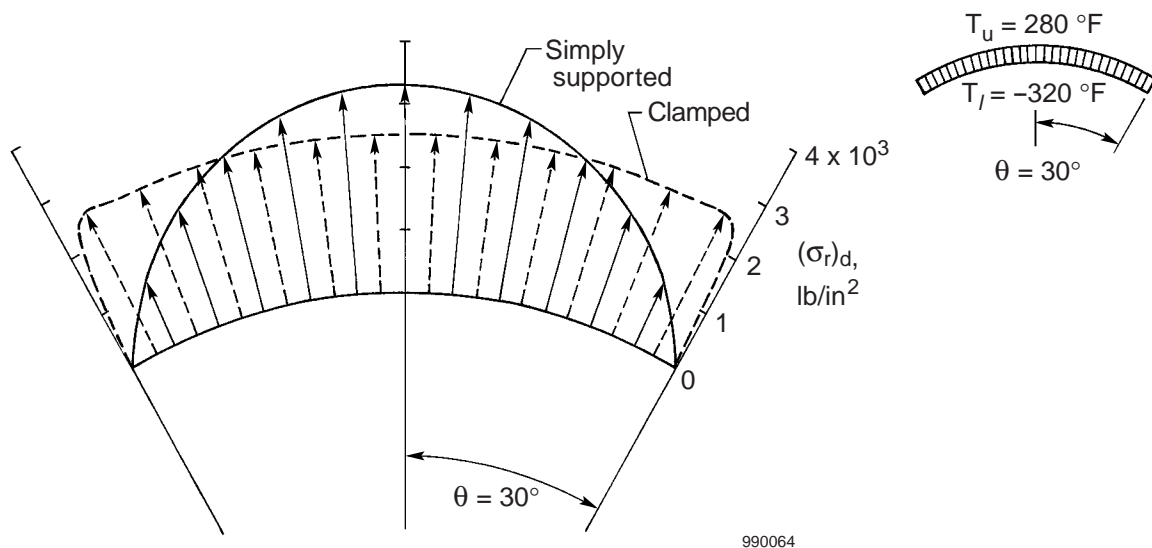
Figure 20. Tangential distributions of local maximum open-mode stress $(\sigma_r)_d$ in curved honeycomb core; $T_u = 280$ °F; $T_l = -320$ °F; $\theta = 30°$.

26
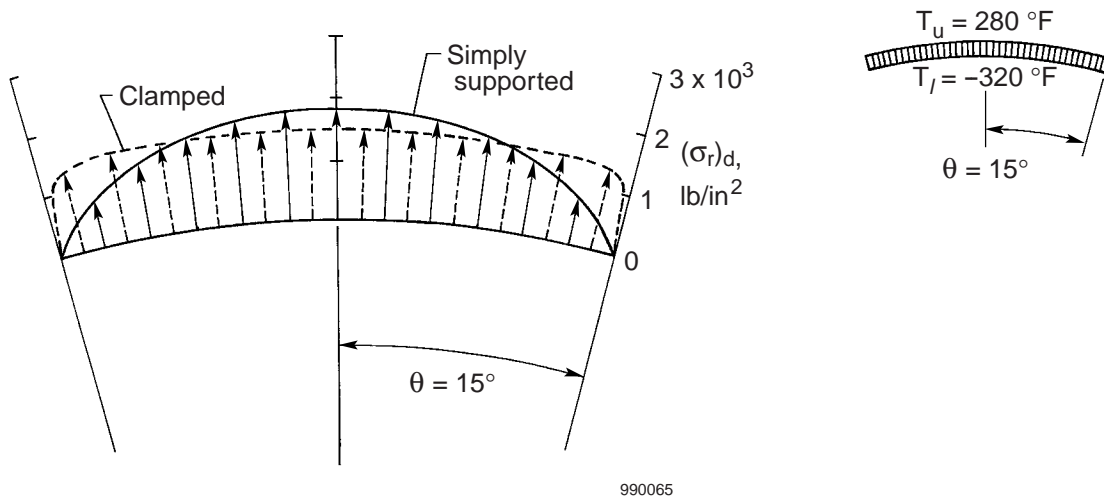
Figure 21. Tangential distributions of local maximum open-mode stress $(\sigma_r)_d$ in curved honeycomb core; $T_u = 280\ °F$; $T_l = -320\ °F$; $\theta = 15°$.
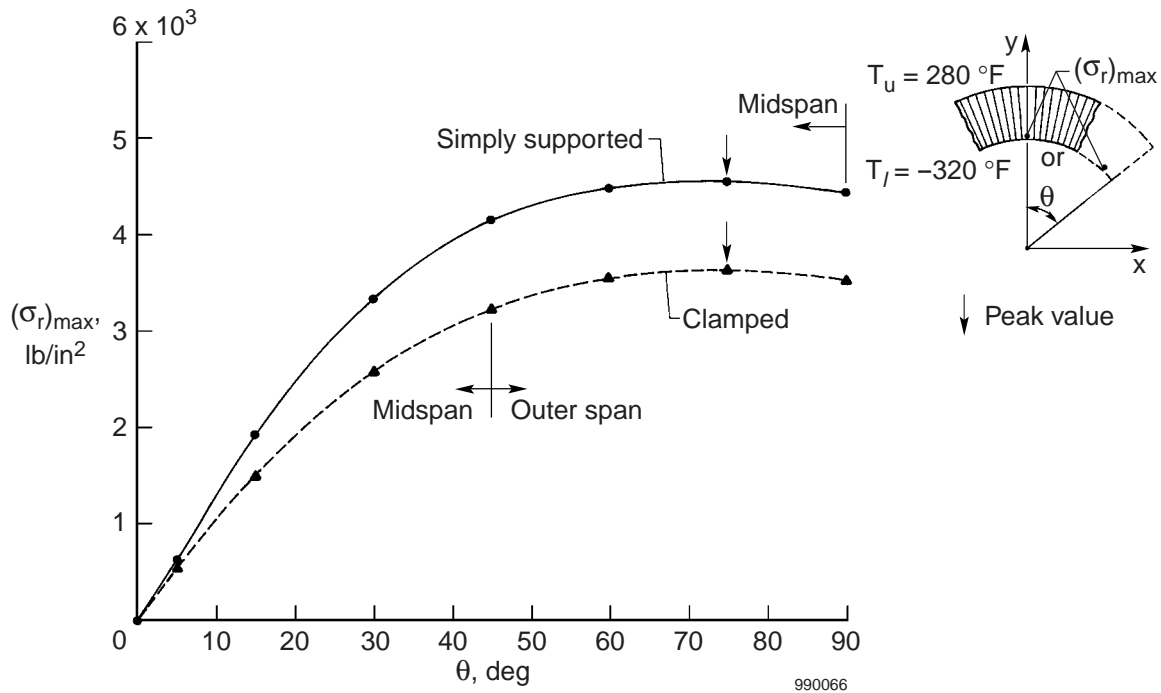
Figure 22. Plots of maximum open-mode stress $(\sigma_r)_{max}$ (at midspan or outer span) as function of curvature angle θ; $T_u = 280\ °F$; $T_l = -320\ °F$.
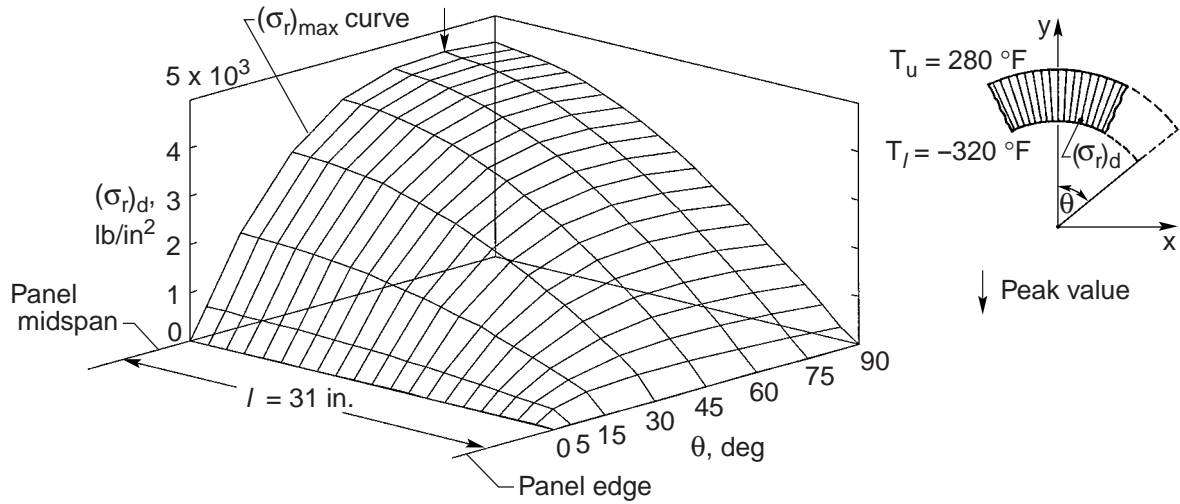
Figure 23. Distribution of local maximum open-mode stress $(\sigma_r)_d$ in the l-θ space; $T_u = 280\ ^\circ\mathrm{F}$; $T_l = -320\ ^\circ\mathrm{F}$; simply supported.
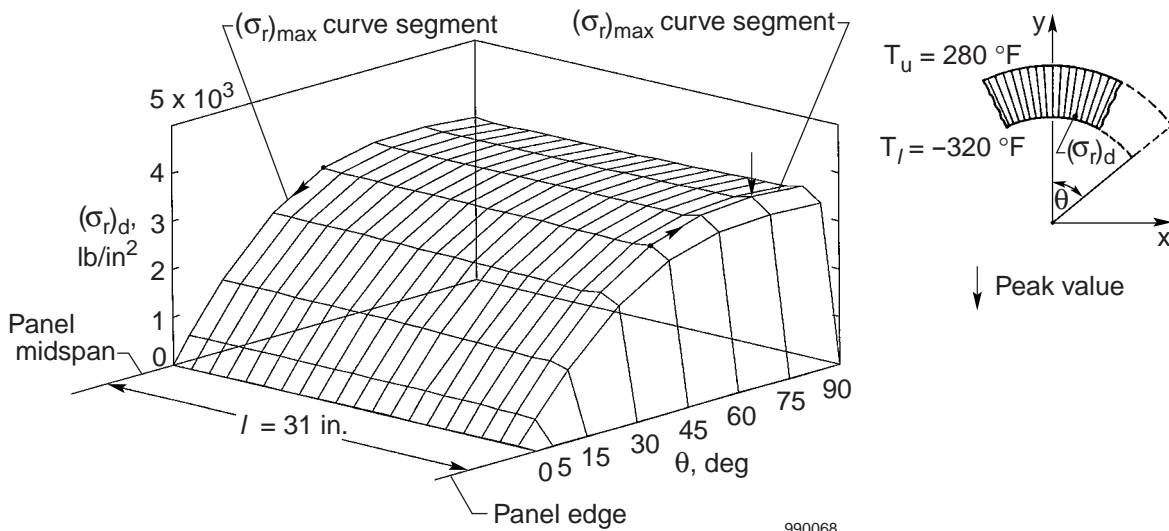
Figure 24. Distribution of local maximum open-mode stress $(\sigma_r)_d$ in the l-θ space; $T_u = 280\ ^\circ\mathrm{F}$; $T_l = -320\ ^\circ\mathrm{F}$; clamped.

28
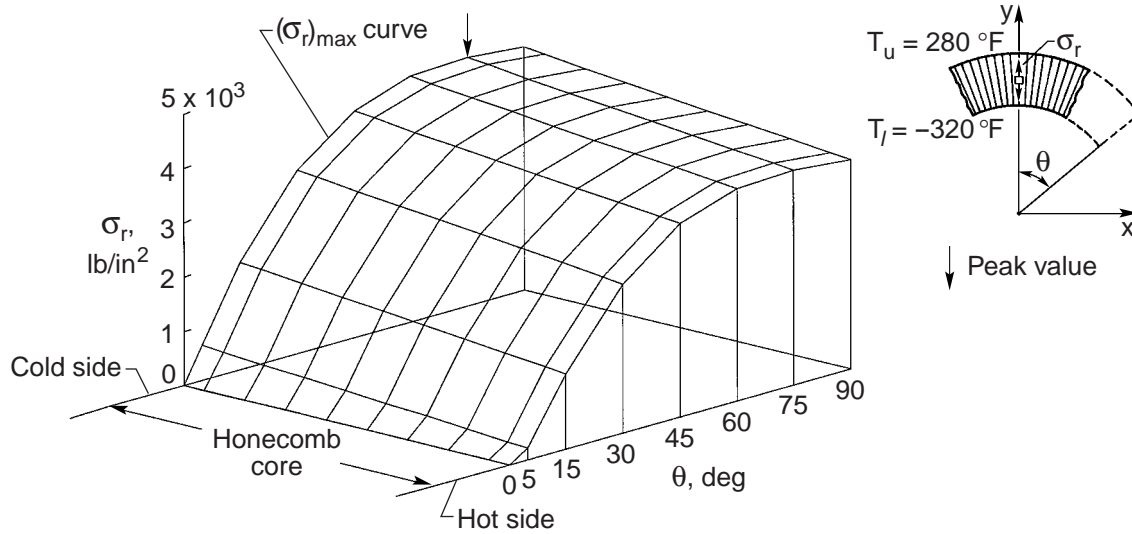
Figure 25. Radial distribution of open-mode stress σ_r along y-axis as a function of curvature angle θ; $T_u = 280$ °F; $T_l = -320$ °F; simply supported.
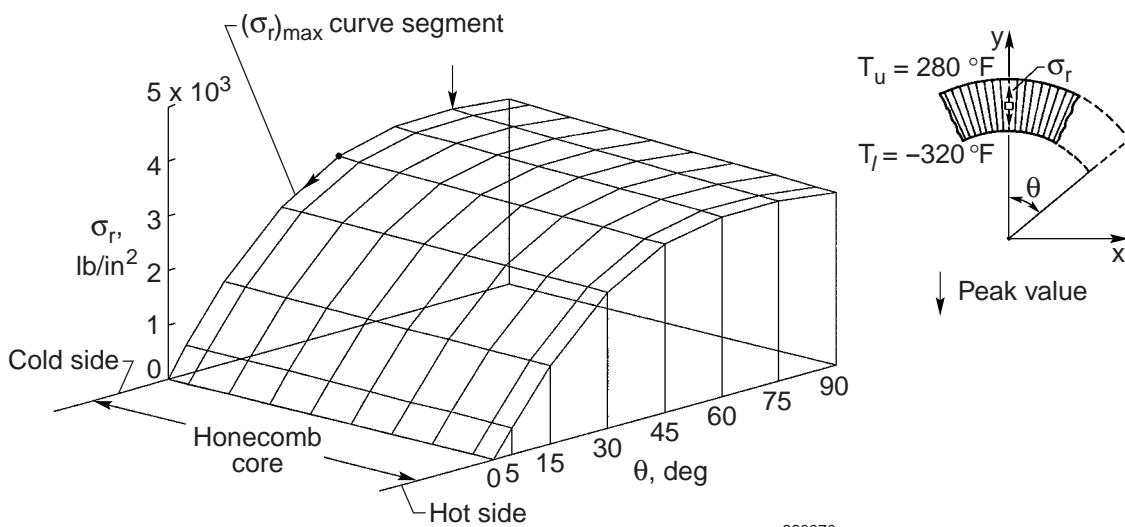
Figure 26. Radial distribution of open-mode stress σ_r along y-axis as a function of curvature angle θ; $T_u = 280$ °F; $T_l = -320$ °F; clamped.
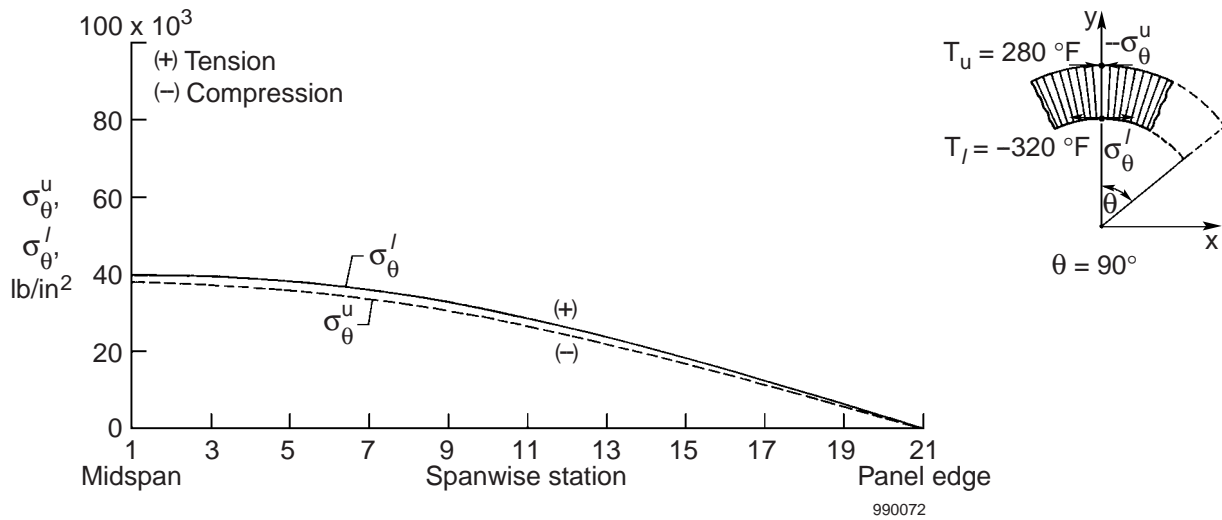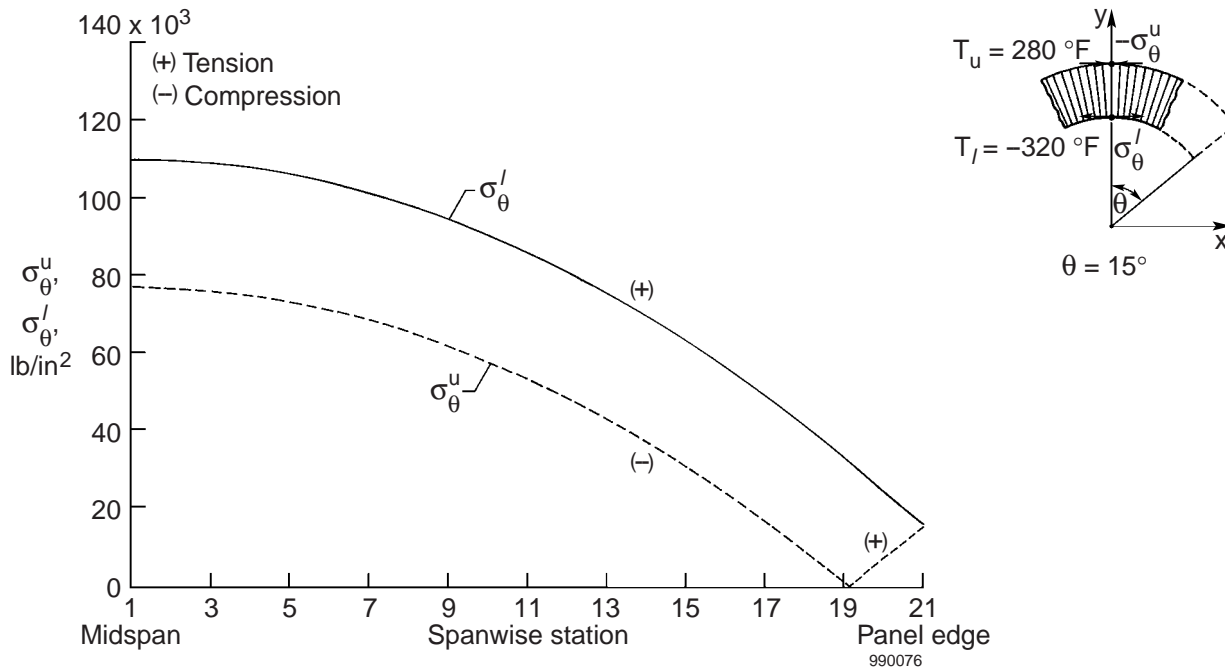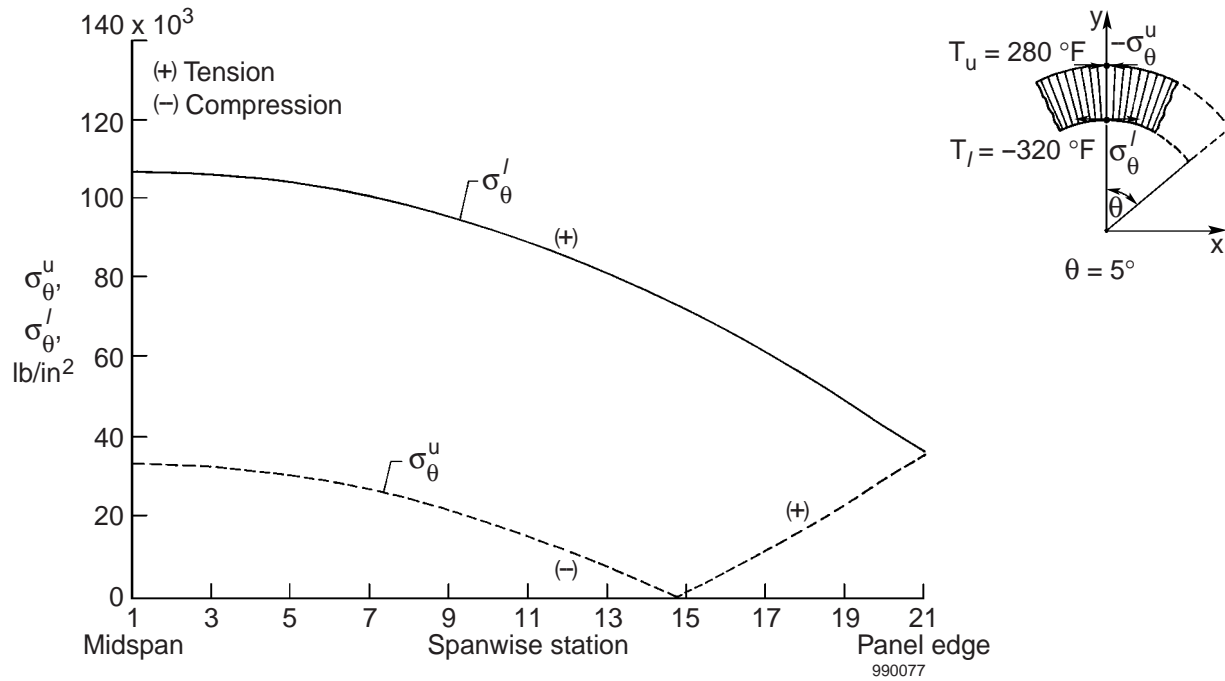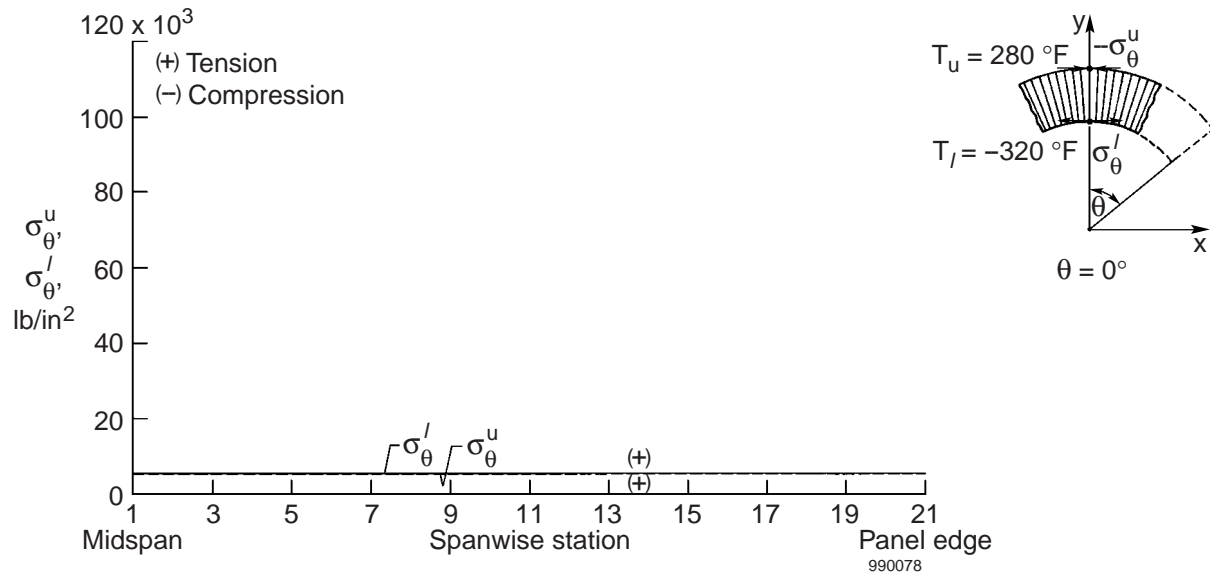
Figure 27. Tangential distributions of tangential stresses $\{\sigma_\theta^u, \sigma_\theta^l\}$ in the face sheets; $T_u = 280\ °F$; $T_l = -320\ °F$; $\theta = 90°$; simply supported.
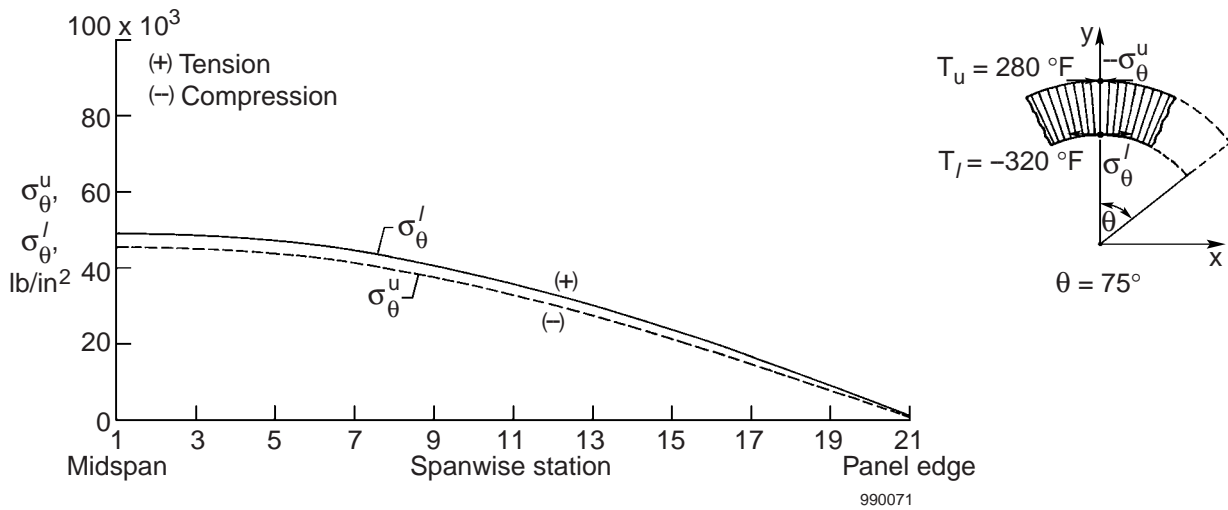
Figure 28. Tangential distributions of tangential stresses $\{\sigma_\theta^u, \sigma_\theta^l\}$ in the face sheets; $T_u = 280\ °F$; $T_l = -320\ °F$; $\theta = 75°$; simply supported.

30
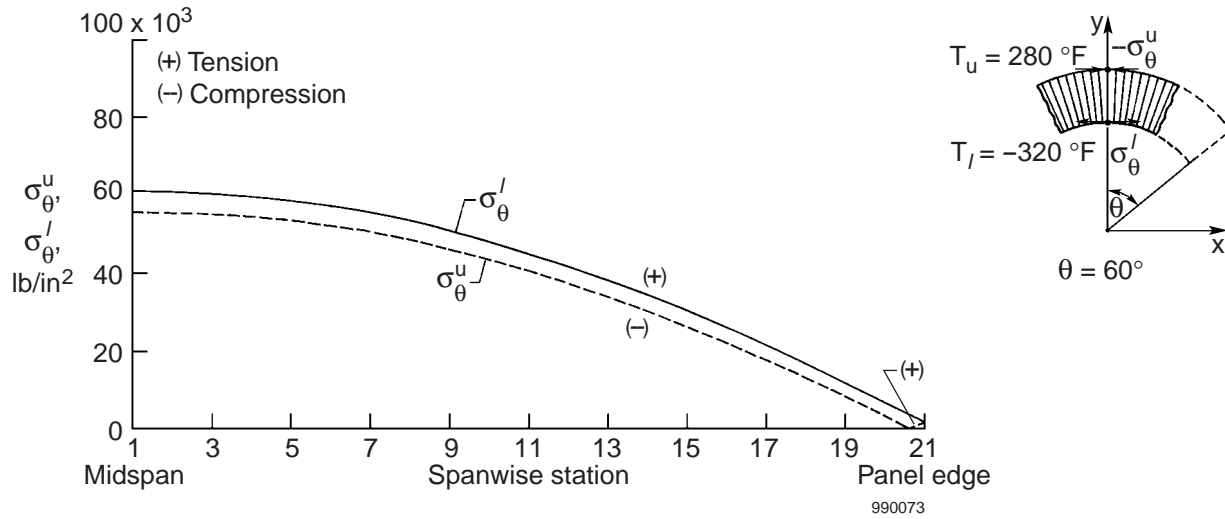
Figure 29. Tangential distributions of tangential stresses $\{\sigma_\theta^u, \sigma_\theta^l\}$ in the face sheets; $T_u = 280\ °F$; $T_l = -320\ °F$; $\theta = 60°$; simply supported.
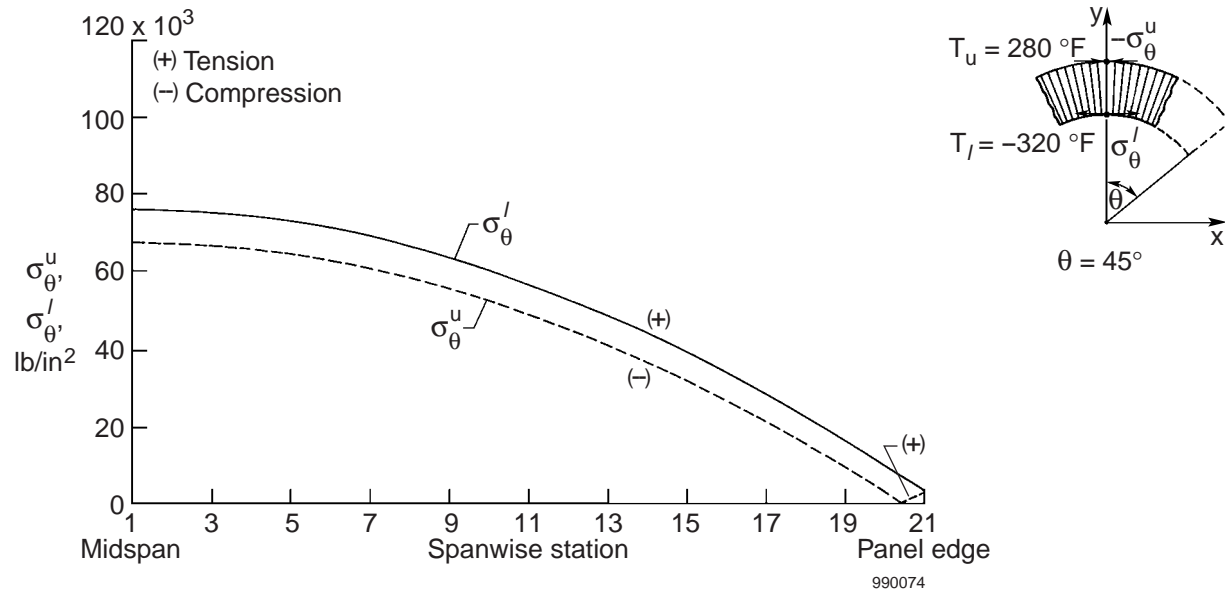
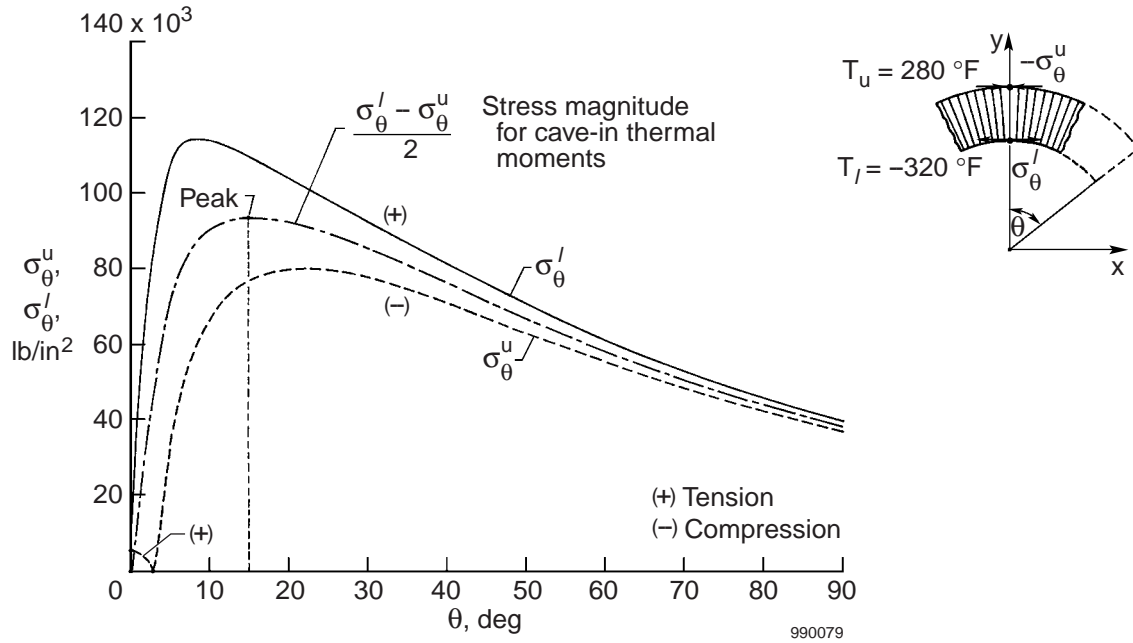Figure 30. Tangential distributions of tangential stresses $\{\sigma_\theta^u, \sigma_\theta^l\}$ in the face sheets; $T_u = 280\ °F$; $T_l = -320\ °F$; $\theta = 45°$; simply supported.
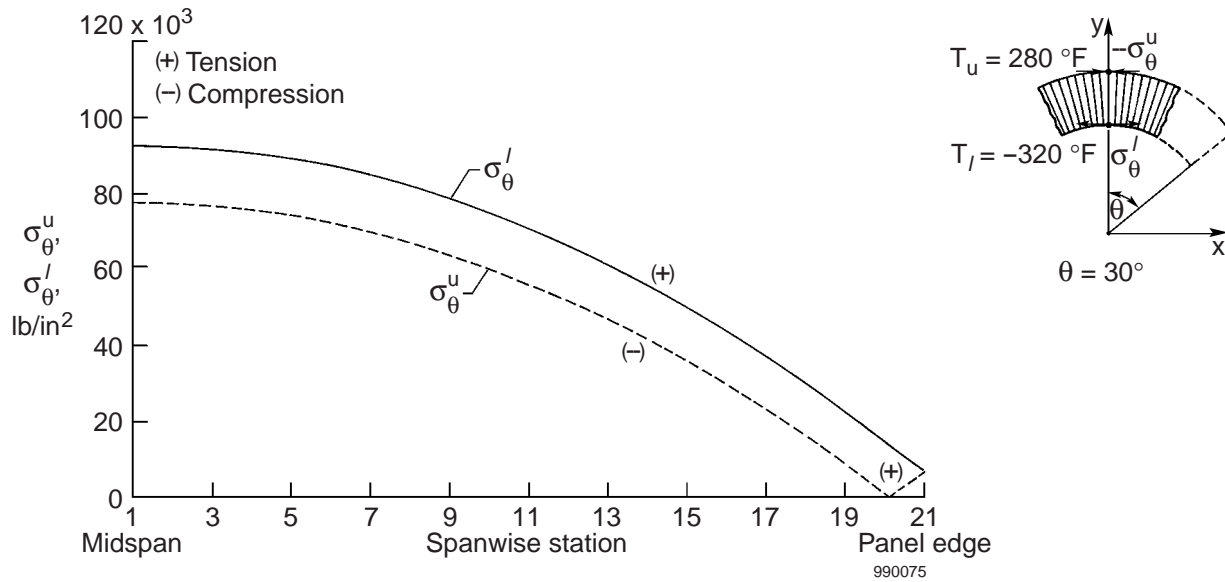
Figure 31. Tangential distributions of tangential stresses $\{\sigma_\theta^u, \sigma_\theta^l\}$ in the face sheets; $T_u = 280$ °F; $T_l = -320$ °F; $\theta = 30°$; simply supported.
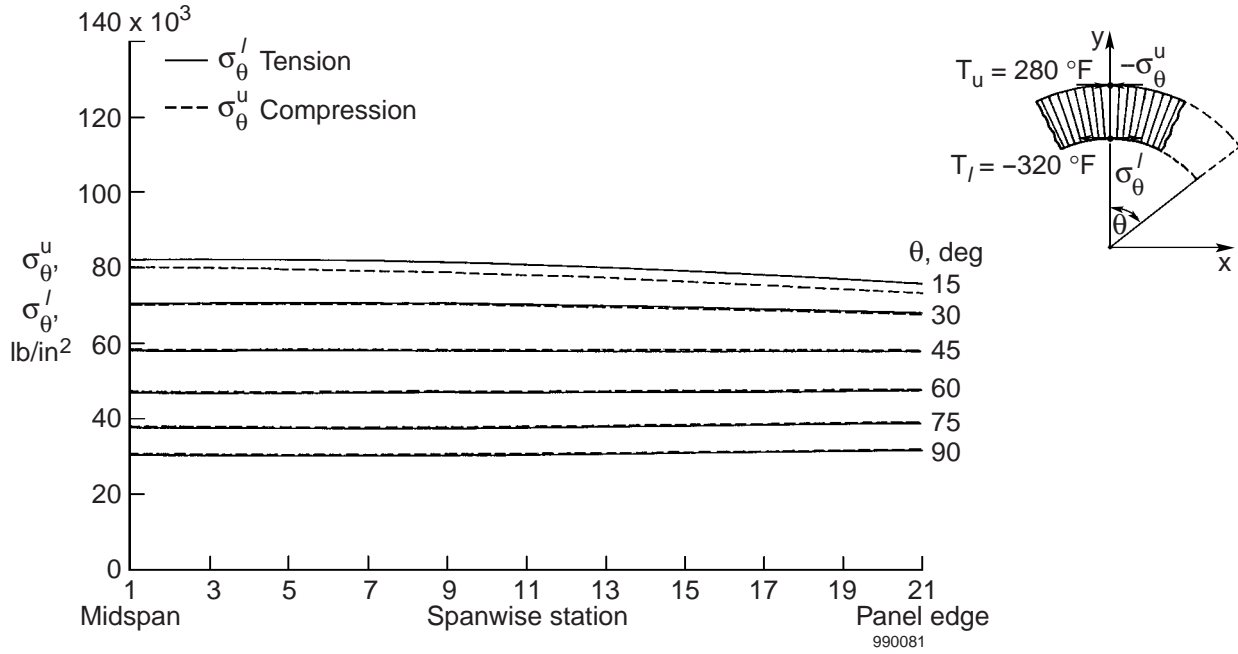

Figure 32. Tangential distributions of tangential stresses $\{\sigma_\theta^u, \sigma_\theta^l\}$ in the face sheets; $T_u = 280$ °F, $T_l = -320$ °F; $\theta = 15°$; simply supported.

Figure 33. Tangential distributions of tangential stresses $\{\sigma_\theta^u, \sigma_\theta^l\}$ in the face sheets; $T_u = 280$ °F; $T_l = -320$ °F; $\theta = 5°$; simply supported.
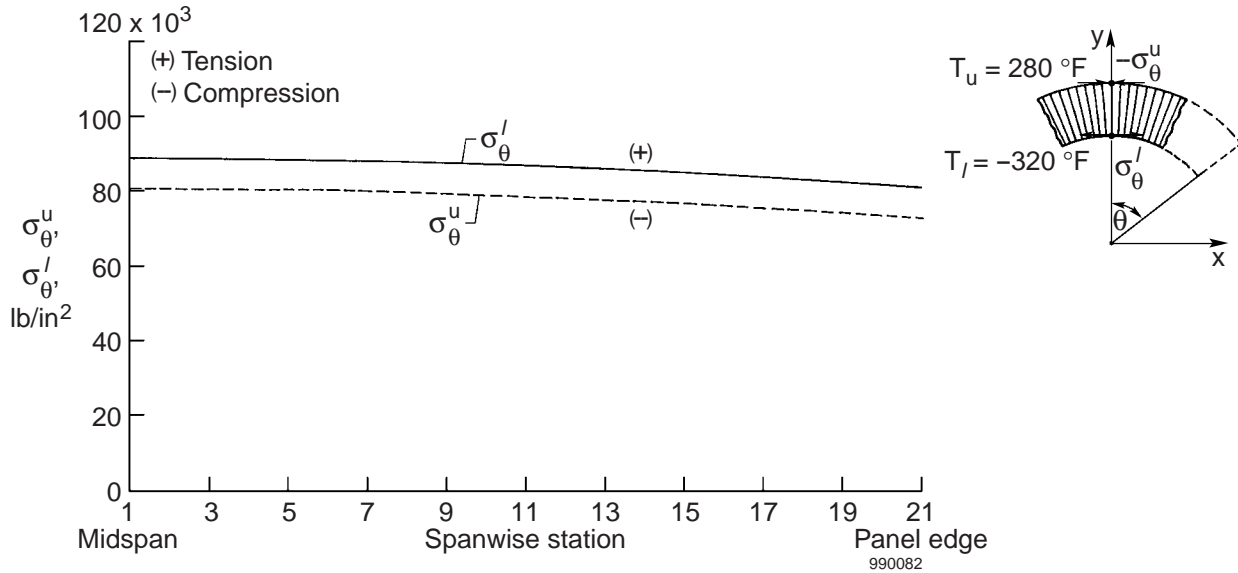

Figure 34. Tangential distributions of tangential stresses $\{\sigma_\theta^u, \sigma_\theta^l\}$ in the face sheets; $T_u = 280$ °F; $T_l = -320$ °F; $\theta = 0°$; simply supported.

Figure 35. Face sheets tangential stresses $\{\sigma_\theta^u, \sigma_\theta^l\}$ at panel midspan as functions of curvature angle θ; $T_u = 280\ °F$; $T_l = -320\ °F$; simply supported.
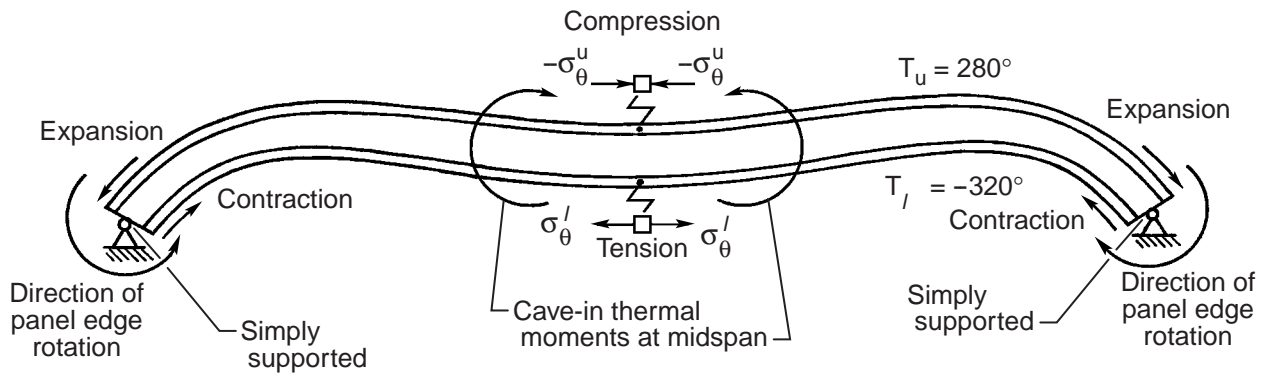
Figure 36. M-shaped deformation of the simply supported curved sandwich panel caused by the combined effect of the cave-in thermal moments induced in the panel and the bowing rotations at the panel edges; $T_u = 280\ °F$; $T_l = -320\ °F$; $\theta = 15°$.
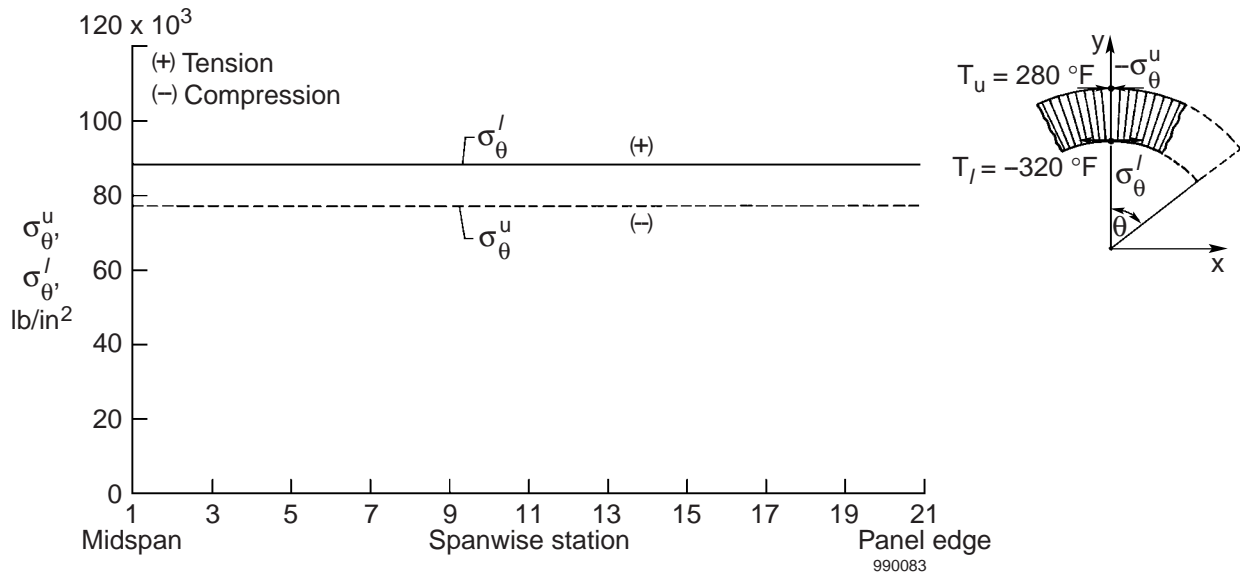
Figure 37. Tangential distributions of tangential stresses $\{\sigma_\theta^u, \sigma_\theta^l\}$ in the face sheets; $T_u = 280$ °F; $T_l = -320$ °F; $\theta = 90°\!\sim\!15°$; clamped.

Figure 38. Tangential distributions of tangential stresses $\{\sigma_\theta^u, \sigma_\theta^l\}$ in the face sheets; $T_u = 280$ °F; $T_l = -320$ °F; $\theta = 5°$; clamped.

Figure 39. Tangential distributions of tangential stresses $\{\sigma_\theta^u, \sigma_\theta^l\}$ in the face sheets; $T_u = 280\ °F$; $T_l = -320\ °F$; $\theta = 0°$; clamped.
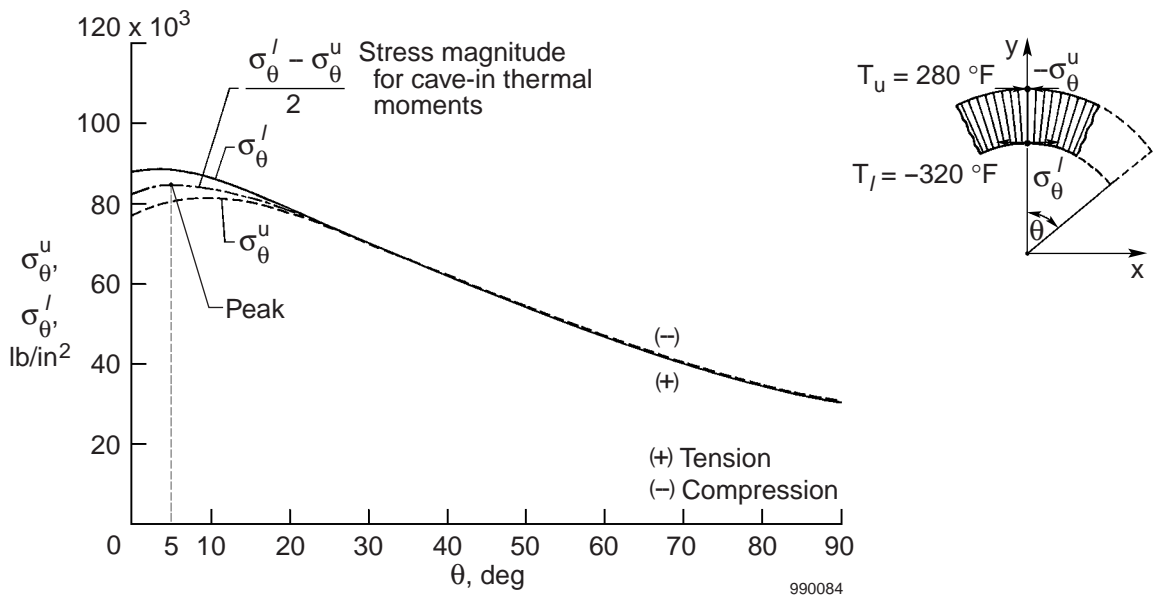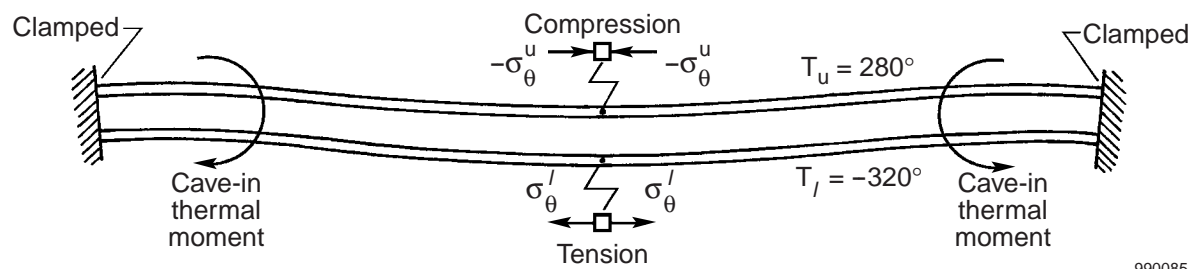

Figure 40. Face sheets tangential stresses $\{\sigma_\theta^u, \sigma_\theta^l\}$ at panel midspan as functions of curvature angle θ; $T_u = 280\ °F$; $T_l = -320\ °F$; clamped.

36

Figure 41. Cave-in deformation of the clamped curved sandwich panel caused by the cave-in thermal moments induced in the panel; $T_u = 280\ °F$; $T_l = -320\ °F$; $\theta = 5°$.

REPORT DOCUMENTATION PAGE

1. AGENCY USE ONLY (Leave blank)	2. REPORT DATE June 1999	3. REPORT TYPE AND DATES COVERED Technical Paper

4. TITLE AND SUBTITLE

Open-Mode Debonding Analysis of Curved Sandwich Panels Subjected to Heating and Cryogenic Cooling on Opposite Faces

6. AUTHOR(S)

William L. Ko

5. FUNDING NUMBERS

WU 242-33-02-00-23-00-TA1

7. PERFORMING ORGANIZATION NAME(S) AND ADDRESS(ES)

NASA Dryden Flight Research Center
P.O. Box 273
Edwards, California 93523-0273

8. PERFORMING ORGANIZATION REPORT NUMBER

H-2332

9. SPONSORING/MONITORING AGENCY NAME(S) AND ADDRESS(ES)

National Aeronautics and Space Administration
Washington, DC 20546-0001

10. SPONSORING/MONITORING AGENCY REPORT NUMBER

NASA/TP-1999-206580

11. SUPPLEMENTARY NOTES

12a. DISTRIBUTION/AVAILABILITY STATEMENT

Unclassified—Unlimited
Subject Category 39

12b. DISTRIBUTION CODE

13. ABSTRACT (Maximum 200 words)

Increasing use of curved sandwich panels as aerospace structure components makes it vital to fully understand their thermostructural behavior and identify key factors affecting the open-mode debonding failure. Open-mode debonding analysis is performed on a family of curved honeycomb-core sandwich panels with different radii of curvature. The curved sandwich panels are either simply supported or clamped, and are subjected to uniform heating on the convex side and uniform cryogenic cooling on the concave side. The finite-element method was used to study the effects of panel curvature and boundary condition on the open-mode stress (radial tensile stress) and displacement fields in the curved sandwich panels. The critical stress point, where potential debonding failure could initiate, was found to be at the midspan (or outer span) of the inner bonding interface between the sandwich core and face sheet on the concave side, depending on the boundary condition and panel curvature. Open-mode stress increases with increasing panel curvature, reaching a maximum value at certain high curvature, and then decreases slightly as the panel curvature continues to increase and approach that of quarter circle. Changing the boundary condition from simply supported to clamped reduces the magnitudes of open-mode stresses and the associated sandwich core depth stretching.

14. SUBJECT TERMS

Curved sandwich panels, Debonding stresses, Open-mode debonding, Thermo-cryogenic loading

15. NUMBER OF PAGES
44

16. PRICE CODE
A03

17. SECURITY CLASSIFICATION OF REPORT Unclassified	18. SECURITY CLASSIFICATION OF THIS PAGE Unclassified	19. SECURITY CLASSIFICATION OF ABSTRACT Unclassified	20. LIMITATION OF ABSTRACT Unlimited